学位論文

A study of the *d-p* elastic scattering at $E_d = 270$ MeV

重陽子–陽子散乱の $E_d = 270$ MeV での研究

平成7年12月 博士（理学）申請

東京大学大学院理学系研究科
物理学専攻

坂本 成彦

A study of the d-p elastic scattering at $E_d = 270$ MeV

Naruhiko Sakamoto

submitted to

Department of Physics
School of Science
University of Tokyo
Bunkyo-ku, Tokyo 113, Japan

for the degree of
Doctor of Science

December, 1995

論文の内容の要旨

論文題目　重陽子-陽子散乱の $E_d = 270$ MeV での研究

氏名　　坂本成彦

1. 序

この研究の動機は、“多核子系の現象、特にスピンに依存する現象は、2体の核力を用いてどの程度記述することができるか” という原子核物理の大局的な興味に因る。多核子系としていろいろな系が考えられるが、その中でも重陽子-陽子散乱、特に中間エネルギー領域 ($E/A \geq 100$ MeV) での重陽子-陽子散乱が以下に挙げる理由により最も興味深い。

- 重陽子-陽子散乱は核子-原子核散乱の考えうる最も簡単な系である。
- 豊富なスピン観測量 (スピン 1 とスピン 1/2 の粒子の散乱) が測定可能である。
- 重陽子の構造そのものが興味の対象 (テンソル力) である。
- 核子-核子相互作用が低いエネルギー領域より比較的良く決まっている。
- 偏極分解能が大きい値を持つ。
- ドブロイ波長が核子の大きさ程度になる為、**インパルス近似**的な非常に簡単な描像で重陽子-陽子散乱を記述できると期待される。

- 重陽子-陽子散乱を **Faddeev** の計算と比べる場合、低いエネルギー領域で計算に取り入れる際に問題になるクーロン力の影響が小さいので厳密な比較を行うことができる。

ところが、これまで適当な実験施設が無かったために、中間エネルギー領域での重陽子-陽子散乱の研究は非常に遅れている。

重陽子-陽子散乱の散乱振幅を全てのスピンの自由度に関して実験的に求めるのは不可能であり、よく分かっている核子-核子散乱の散乱振幅を用いて重陽子-陽子散乱を簡単なモデルで記述できるとすると、例えば中間エネルギーでの重陽子-核子散乱の解析を行うのに非常に有用である。

Faddeev の計算は、低いエネルギー領域でのデータをあまりよく再現しないことが知られている。その理由はひとつにはクーロン力の取り扱いが難しい為である。クーロン力の影響が小さく、かつ、核子-核子相互作用が比較的良く分かっている中間エネルギー領域で実験と計算の比較を行うことは有意義であると考える。

そこで我々は、270 メガ電子ボルトの重陽子ビームを用いた重陽子陽子散乱の精度の良い実験を行い、2つの理論計算、インパルス近似と Faddeev 計算、との比較を行った。偏極重陽子-陽子散乱の散乱微分断面積は、

$$\frac{d\sigma_{\rm pol}(\theta)}{d\Omega} = \frac{d\sigma_{\rm unpol}(\theta)}{d\Omega}\Big[\, 1 + \frac{3}{2}p_y\, A_y(\theta) + \frac{2}{3}p_{xz}\, A_{xz}(\theta) + \frac{1}{3}(p_{xx}\, A_{xx}(\theta) + p_{yy}\, A_{yy}(\theta) + p_{zz} A_{zz}(\theta))\,\Big] \,.$$

と表される。ここで、$\frac{d\sigma_{\rm unpol}(\theta)}{d\Omega}$ は、ビームが偏極していないときの微分散乱断面積、p は重陽子の偏極を表す。A が偏極分解能で、$A_{xx}+A_{yy}+A_{zz}=0$ を満たす。測定したのは、微分散乱断面積と独立な全ての偏極分解能、A_y、A_{yy}、A_{xx}、A_{xz} であり、中間エネルギー領域では世界で初めての測定である。

我々はこの実験に先立って、大強度、高偏極度の偏極イオン源 (図 1)、標的上でのスピンの向きを任意に制御できるスピン制御システム、ビーム偏極度を測定するための偏極度計の開発、整備を行って来た。中でも偏極イオン源は、偏極度 80%、ビーム強度 100 μA を達成しており世界最高水準の性能を持つ。

2. 実験

実験はサイクロトロンによって 270 メガ電子ボルトまで加速された重陽子ビームを用いて行った。測定量は、$\frac{d\sigma_{\rm unpol}(\theta)}{d\Omega}$、$A_y(\theta)$、$A_{yy}(\theta)$、$A_{xx}(\theta)$、$A_{xz}(\theta)$ で測定範囲は、重心系の角度で 57 度から 138 度である。この角度範囲は、他のエネルギーでのデータから微分散乱断面積が最小になりかつ偏極分解能が比較的大きい値をとることが予想される領域である。標的はポリエチレン (CH_2) 膜を用いた。偏極ビームの偏極度の絶対値は、${}^{12}C(d,p){}^{13}C_{\rm gnd}(E_d = 14{\rm MeV})$ のデータを元に較正された。

重陽子-陽子散乱の非対称性を上下左右方向に検出器を配置し、偏極・非偏極

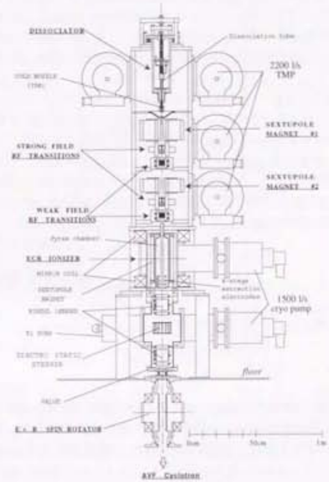

図 1: 偏極イオン源

ビームを用いて測定した。散乱重陽子と反跳陽子を、運動学の計算によって求めた角度に検出器を配することにより同時に計測した。検出器は、プラスチック検出器 (NE102a 1 cm^t+H1161) を用いた。角度の分解能は、陽子検出器によって決まり、$\Delta\theta_p = \pm 1.14°$である (重心系に直すとほぼ二倍)。重陽子-陽子散乱は、散乱粒子の検出器でのエネルギー損失及び標的からの飛行時間の情報によって識別され、信号雑音比は 200 から 300 程度であった。

偏極分解能は、測定した上下左右の散乱の非対称から得られる。A_y、A_{yy}、A_{xx}は、スピンの向きが鉛直方向を向いたビームを用いた計数率から、A_{xz}は水平面内 45 度にスピンを傾けたビームでの計数率から求められる。測定結果を図2に黒丸で示す。特徴的なのは、ベクトル偏極分解能 A_yが、60 度と 140 度でゼロを横切るのに対して、テンソル偏極分解能は一定の符号の大きな絶対値を持つことである。誤差は、統計誤差が約±3%以下、系統誤差が±2%(偏極度の

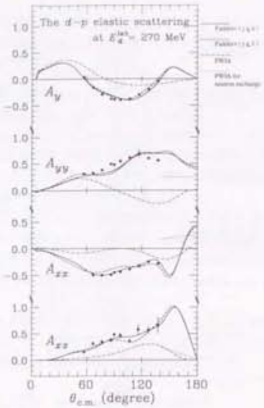

図 2: 重陽子–陽子弾性散乱 ($E_d = 270$ MeV) の偏極分解能。実線、破線、一点鎖線、点線は、それぞれ Faddeev 計算の核子-核子全角運動量が 4 までと 3 までの結果、インパルス近似による直接弾性過程、中性子移行過程の計算値。

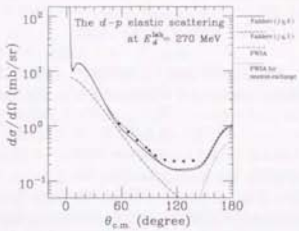

図 3: 重陽子–陽子弾性散乱 ($E_d = 270$ MeV) の微分散乱断面積。実線、破線、一点鎖線、点線は、図 2に同じ。

絶対値の較正)、A_{xz} に関しては更に±2%(スピンの角度)、である。

微分散乱断面積の測定は、非偏極ビームを用いて独立に行った。偏極分解能の測定と同様に、重陽子と陽子の同時計測法を用いた。測定結果を図 3に黒丸で示す。誤差は、統計誤差が±1%、系統誤差が±2%(標的厚み) ±3%(測定系) ±5%(電荷量) である。

炭素標的の陽子ノックアウト反応は、その出射粒子が重陽子-陽子弾性散乱と同じため重陽子–陽子散乱との区別ができない。標的としてポリエチレン (CH_2) を用いたので、標的中の炭素の影響を調べる必要がある。そこで微分散乱断面積の測定に際し、炭素標的に対して重陽子–陽子の重心系の角度 86.6 度のセットアップで同時計測されるイベントの計数率を測定した。その結果、ポリエチレン標的中の炭素の影響は、測定された重陽子-陽子散乱の微分散乱断面積に対して 1%以下であることが分かった。これにより、偏極分解能への影響も十分小さいということが言える。

3. 理論計算との比較と考察

実験データとインパルス近似、Faddeev 計算の 2 つのモデルによる計算値との比較を行った。

インパルス近似

重陽子の中の一つの核子が標的陽子と一度だけ散乱するという非常に簡単な描像での重陽子-陽子散乱の散乱行列を核子-核子散乱の散乱振幅を用いて求めた。この過程の散乱行列を求める際、重陽子の中の散乱に関わる核子の運動量の広がりをある運動量で代表させるという近似 (因子化近似) を行った。計算結果を図 2、3 に一点鎖線で示す。簡単のため、中性子交換反応、重陽子の D状態の効果は無視した。比較の結果、微分散乱断面積の形は 90 度より前方で概ね再現されているが他の観測量の再現性はあまりよくないことがわかった。そこでこの計算で無視された効果のうち、中性子交換反応に関して考察を行った。重陽子の中の中性子が標的陽子に移行して重陽子になるという過程に関してその散乱振幅を求めて微分散乱断面積及び重陽子偏極分解能を求めた。結果を点線で示す。この反応過程は、後方角でおおきな断面積を持つことがわかった。しかしながら、この過程を考慮しても微分散乱断面積が最小になる領域での断面積の絶対値を再現することはできない。我々の測定範囲で、データの再現性を良くするためには、計算で無視された他の効果、特に重陽子の D状態を考慮する必要があると考えられる。

Faddeev 計算

Faddeev の理論は、二体の相互作用を用いて三体系を厳密に記述する。図 2、3に実線で示した三体計算の結果 (実線及び破線) は小池氏(法政大) により分離型ポテンシャル法で三体の Faddeev 方程式を解いて得られたものである。核子-核子相互作用としては Argonne v_{14}が用いられ、核子-核子間の全角運動量が 4 の

成分まで計算に取り入れられた。低エネルギー領域では、実験データの再現性が良くないのに対し、270 メガ電子ボルトでは、特に偏極分解能が非常によく再現されることが分かった。Faddeev 計算の結果を詳しくみてみると、偏極分解能が非常によく再現されているのに対して、微分散乱断面積はその値が最小となる 90 度から 140 度で計算値が最大 30%ほど小さくなっている。また、重陽子のエネルギーで 130 メガ電子ボルトと 190 メガ電子ボルトに相当するエネルギーに対して行った同様の計算結果と存在する実験データとを比べて見ると、これらのエネルギーでも計算値が同程度に実験値より小さくなることがわかった。この不一致の理由は未だ明らかになっていない。この計算で考慮されていない、三体力や相対論の効果が断面積や偏極分解能にどの程度寄与するかは興味のあるところである。

4. 結論と今後の課題

中間エネルギー領域で初めて、重陽子-陽子散乱の微分散乱断面積と全ての偏極分解能の高精度のデータを得た。

最初にその実験結果とインパルス近似の計算との比較を行った。微分散乱断面積が 90 度より前方で概ね再現されたものの、他の観測量については再現性はよくなかった。本論文では取り入れなかった重陽子の D 状態がどの程度効くのかを調べるのは今後の課題である。

Faddeev 計算との比較では、非常に良い再現性が得られた。低エネルギー領域での状況を考えると非常に興味深い。しかしながら、断面積が最小になる部分で 30%程度の不一致が見られた。この事は、Argonne v_{14} に問題があるか、あるいは Faddeev 計算に何らかの、例えば三体力を取り入れる等の変更を要することを示唆する。また、昨今話題になっている、相対論的な効果や中間状態でデルタを生成するチャンネルの効果が微分散乱断面積にどの程度現れるかも興味のあるところである。

Contents

List of Figures

Chapter 1

Introduction

1.1 Introduction

The deuteron-proton (d-p) scattering at intermediate energies ($E/A \geq 100$ MeV) is a particularly good source of information on the spin-dependent nucleon-nucleon (NN) interaction. The spin-dependent forces are strong and manifest themselves mainly through the polarization observables. Due to the spin-structure 1-$\frac{1}{2}$, there exist various polarization observables for the d-p scattering. Since magnitudes of polarization observables for the d-p scattering become large with the increase of the scattering energy, the d-p scattering at intermediate energies is a convenient means for the study of the spin-dependent forces.

Since the small binding energy of the deuteron produces a rather large separation distance between its constituent proton and neutron, the d-p scattering can be well described by a scattering model whose fundamental scattering process is the two-body NN scattering. Furthermore, since the wave-length of the target proton in the deuteron rest frame becomes as small as the size of nucleon, the single scattering process in which one of the constituent nucleons of the deuteron undergoes a single scattering with the target proton becomes dominant in the d-p elastic scattering at intermediate energies. Therefore it is interesting to study how well the d-p scattering can be described by the single scattering description, which is generally called as an impulse approximation (IA), utilizing the NN scattering amplitudes obtained from a

number of the experimental data on the NN scattering.

Such a study is also helpful to understand the various spin-dependent phenomena of the deuteron induced reactions at intermediate energies, for example, the d-p elastic scattering at backward angles, the deuteron elastic scattering, the isoscalar spin-excitation by the deuteron inelastic scattering, and the spin-isospin excitation by the (d,^{2}He) reaction. The analyzing powers, which represent the deviation of the differential cross sections with polarized beam from that with unpolarized beam, are closely related to various physics interests [1] as follows:

- The tensor analyzing power T_{20} for the d-p elastic scattering at 180° is served for the study of the deuteron structure. In the plane wave impulse approximation (PWIA), T_{20} at 180° is directly related to the D-state to S-state ratio of the deuteron wave function [2].
- Three types of the tensor interactions i.e. the coordinate dependent, the angular-momentum dependent, and the momentum dependent tensor interactions can be investigated through the tensor analyzing powers A_{zz} and A_{xz} for the deuteron elastic scattering at intermediate energies [3].
- Deuterons have spin 1 and iso-spin 0 so that the deuteron inelastic scattering possesses selectivity of $\Delta S = 0, 1, 2$ and $\Delta T = 0$. Hence, the deuteron inelastic scattering is particularly a good probe to study the isoscalar spin excitation of the nucleus whose origin is the spin-spin interaction term of the NN interaction [4].
- The (d,^{2}He) reaction[1], which is (n,p)-type charge exchange reaction, is a powerful probe to study the spin-dipole excitation ($\Delta S = 1$, $\Delta L = 1$) of the nucleus. From the predictions of PWIA calculations, the states of the spin-dipole excitation can be resolved into the substates of the spin-parity $j^\pi = 2^-, 1^-$, and 0^-

[1] ^{2}He is two emitted protons coupled to the singlet S state.

by observing the tensor analyzing powers A_{yy} and A_{zz} for the $(d,{}^2\mathrm{He})$ reaction [5].

This favorable situation is considered to be due to the fact that the reaction mechanism becomes simple at intermediate energies. Since the deuteron wave-length becomes as small as the size of the nucleon, the deuteron-nucleon single scattering process is expected to be be dominant in these reactions at intermediate energies. Thus the d-p scattering is important as a fundamental process in describing the deuteron induced reactions at intermediate energies.

1.2 Analyzing powers for the polarized deuteron scattering

Analyzing powers for the scattering of the polarized beams are obtained by measuring the ratios of the scattering yields. Typical ratios might be "left-right" and "up-down" asymmetries, or polarized beam to unpolarized beam yield ratios.

For the scattering of the polarized deuteron beams whose spin is 1, the most general form of the differential cross sections is written as:

$$\begin{aligned}\frac{d\sigma_{\mathrm{pol}}(\theta)}{d\Omega} = \frac{d\sigma_{\mathrm{unpol}}(\theta)}{d\Omega}[\ 1 \ &+\ \frac{3}{2}p_y\, A_y(\theta) + \frac{2}{3}p_{xz}\, A_{xz}(\theta) \\ &+\ \frac{1}{3}(p_{xx}\, A_{xx}(\theta) + p_{yy}\, A_{yy}(\theta) + p_{zz}\, A_{zz}(\theta))\ ]\ . \quad (1.1)\end{aligned}$$

The coefficients p's are the polarizations of the incident deuterons and the A's represent the analyzing powers for the polarized deuteron scattering. These properties are defined in the Cartesian coordinates of $\hat{\vec{z}} \,//\, \vec{k}_i$, $\hat{\vec{y}} \,//\, \vec{k}_i \times \vec{k}_f$, and $\hat{\vec{x}} \,//\, \hat{\vec{y}} \times \hat{\vec{z}}$, where $\vec{k}_i$ and $\vec{k}_f$ are the incident and the scattered deuteron momenta, respectively (Details are described in Appendix A.). In general, an incident beam may have vector polarization components p_x, p_y, and p_z, but because of parity conservation through the reaction process, the reaction is sensitive only to the component normal to the scattering plane so that A_x and A_z are zero. Similarly, although an incident beam

may contain all six tensor polarization components p_{xy}, p_{xz}, p_{yz}, p_{xx}, p_{yy}, and p_{zz}, the reaction is sensitive, again because of parity conservation, only to those indicated in Eq. (1.1).

The tensor analyzing powers A_{xx}, A_{yy}, and A_{zz} satisfy the following relation

$$A_{zz} = -(A_{xx} + A_{yy}) \quad (1.2)$$

so that there remain four independent observables of

$$A_y,\quad A_{yy},\quad A_{xz},\quad \text{and} \quad A_{xx}\ .$$

The analyzing powers contain various information of spin-dependent interactions. The component of the analyzing powers normal to the scattering plane A_y and A_{yy} are sensitive mainly to the spin-orbit $\vec{L}\cdot\vec{S}$ force. The A_{xx} and A_{xz} have physically much more interesting information such as the tensor interaction or the D-state of the deuteron wave function. The measurement of A_{xx} and especially A_{xz} is very difficult since it requires to rotate the deuteron spin to an appropriate angle at the target point. Usually the control of the spin orientation of the beam to the arbitrary direction is not easy. In this work, A_{xz} and A_{xx} have been successfully obtained by a new method of the spin control for the cyclotron laboratory.

1.3 Historical background for studies of the d-p scattering at intermediate energies

There is a wide interest in how well few-nucleon systems can be described by using NN interactions determined by NN scattering data. Among the few nucleon systems, the d-p scattering should be recognized to be be studied at the beginning since it is the simplest possible reaction between nucleon and nucleus. A number of the vector and tensor analyzing powers are useful to examine the NN interaction especially for the spin dependent part, e.g. the spin-orbit force and the tensor force.

In the high energy region such as the incident deuteron energy (E_d^{lab}) [2] of 1-2 GeV, the experiments of polarized proton scattering from polarized deuteron target at 0.8 GeV incident proton energy (E_p^{lab}) were made by the LAMPF group [6] and the experiments of the polarized deuteron scattering from hydrogen target at E_d^{lab} = 1.2, 1.6, and 2.0 GeV were made by the Argonne group [7]. Many kinds of spin observables were measured at the momentum transfer range of $q \leq 1$ GeV/c. The data are compared with a modified Glauber model [8]. The effects due to large scattering energy such as the delta intermediate states and double scattering process have been reported to be important to reproduce the experimental data.

In the low energy region, $E_d^{lab} \leq 100$ MeV, proton and deuteron polarization observables for the d-p elastic scattering have been measured extensively with high accuracy. Recent review of the study on the few-body systems has been made by Glöckle in Ref. [10]. The highly accurate data are compared with the theoretical predictions of Faddeev theory. The three-nucleon system can be described exactly, in principle, by a Faddeev theory [9] if two-body NN interactions are known. However, the fit of the Faddeev calculations with realistic NN potentials is not satisfactory especially for the vector analyzing powers at energies, $E_d^{lab} \leq 30$ MeV where the treatment of the Coulomb force frequently gives ambiguity in the calculations. On the other hand, at high energy region, the effect of the Coulomb distortion becomes less important so that an accurate comparison between experimental data and calculations becomes possible. Consequently, it is interesting to compare the experimental data with the Faddeev calculations at intermediate energy. Such a study will give us information on the effects due the delta degrees of freedom, relativity, and higher partial wave components of the NN interaction. At present, the experimental data of the spin observables for the d-p elastic scattering at high energy region are scarce. At a deuteron incident energy of 187 MeV, the comparison between the data and

[2] $E_d^{lab} = 2E_p^{lab} = 3E_{c.m.}$

the Faddeev calculations has been made [11]. However, the accuracy of the data is not good enough to compare in detail. Thus the experimental data of the d-p elastic scattering with high accuracy at an intermediate energy are needed for the detailed study on the d-p scattering in terms of the Faddeev calculation.

1.4 Aim of this thesis

In the present experiment, the differential cross sections and all components of the analyzing powers A_y, A_{yy}, A_{xx}, and A_{xz} for the d-p scattering have been measured at $E_d^{lab} = 270$ MeV. This is the first measurement of the deuteron analyzing powers with high statistical precision at an intermediate energy.

The ultimate goal of this work is to clarify how well few-nucleon systems can be described by using NN interaction determined from NN scattering data. In this work it is tried to examine how well the experimental data at $E_d^{lab} = 270$ MeV can be reproduced by two models of the PWIA calculation and the three-body Faddeev calculation [3].

The scattering amplitude for the single scattering description is obtained by the PWIA calculation. The PWIA has been successfully applied to the the ^{1}H(d,^{2}He) reaction at $E_d^{lab} = 200$ MeV for the momentum transfer ranges of $q \leq 400$ MeV. Our data cover the momentum transfer range of q = 350 - 650 MeV/c. The predictions of the single scattering description of the d-p elastic scattering are compared with the data at a rather large momentum transfer region where the analyzing powers are expected to have large values.

The Faddeev calculations are compared with the experimental data at an intermediate energy for the first time. As the energy increases, it is needed to include higher partial waves of the NN interaction in the calculation. Calculations are, up to

[3] Three-body Faddeev calculations presented in this thesis were made by Dr. Koike.

now, made employing an NN interaction of total angular momentum $j \leq 3$ since the inclusion of higher partial waves require considerable computing power. In this work, three-body calculations with $j \leq 3$ and ≤ 4 are presented to see the contribution of higher partial waves of $j = 4$ to the differential cross sections and the analyzing powers. It is also interesting to see whether some discrepancies found in the low energy region [13, 14, 15] are also found at $E_d^{\mathrm{lab}} = 270$ MeV or not.

1.5 Preparation of the polarized deuteron beam for physics experiments at an intermediate energy

The RIKEN accelerator research facility (RARF) has an accelerator complex which consists of an injector AVF cyclotron and a main ring cyclotron (see Fig. 1.1). The ring cyclotron has a large K-number of 540 so that deuteron beams can be accelerated up to an energy of 270 MeV. This is the highest energy deuteron beam produced by the cyclotrons in the world. Therefore, RARF is a suitable and a unique facility to study the spin-dependent phenomena by using the deuterons at intermediate energies.

The construction of the polarized ion source at RIKEN started at the end of 1990. The source is an atomic beam type with ECR ionizer whose original design was close to that of HIPIOS at IUCF [16]. HIPIOS was based on the source at TUNL [17]. Many modifications from the original design have been made to the RIKEN polarized ion source and consequently the performance of the source of beam intensity of 140 μA at the ion source exit with 80 % [4] polarization of the ideal value has been achieved [25].

Simultaneously, preparation of the spin control system was made in order to measure the analyzing powers A_{zz} and A_{xz} which contain various information such as the tensor interaction. For an intermediate energy deuteron, the spin rotation sys-

[4] At the time when this experiment was made, the achieved polarization was 60- 70%.

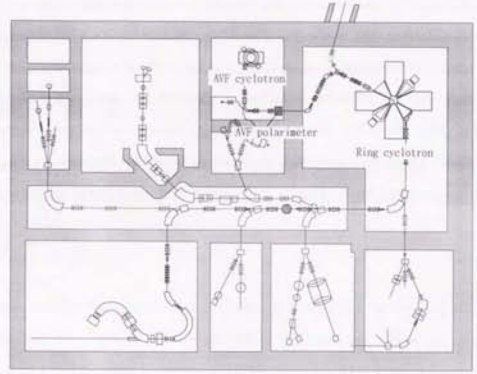

Figure 1.1: RIKEN Accelerator Research Facility

tem becomes extraordinary large due to the small magnetic moment of the deuteron. At RIKEN the spin orientation control is made with a unique technique with Wien filter which is commonly employed at the Van de Graff accelerators. The spin axis is rotated by a Wien filter which is located in the injection line to the AVF cyclotron. This method has been considered unsuitable to the cyclotron accelerators, since the single-turn extraction of the beam from the cyclotron is required to maintain the polarization of the beam. During the acceleration, the deuteron spin precesses along the cyclotron field (Larmour precession). Because the g-factor of the deuteron is 0.8457, the spin orientation β with respect to the beam differs turn by turn[5]. Therefore, the polarization amplitude will be reduced if the deuterons which have different spin orientations are simultaneously extracted from the cyclotrons. The RIKEN cyclotrons can extract the single-turn beam so that the polarization amplitude is maintained.

[5] $\Delta\beta = 360 \times (0.8457 - 1)\ \gamma$ deg./turn. Here, γ is the ratio of the total energy to the deuteron rest mass.

It is also important to measure efficiently the polarization of the accelerated beam in order to determine the final orientation of the spin on the target. Although the deuteron polarimeter at intermediate energies is not well established, the most probable candidate for the polarization analyzer is the elastic scattering on the hydrogen target [18]. Thus, one of the purposes of the present experiment is to examine whether the d-p elastic scattering is usable or not for the polarization analyzer.

Chapter 2

Measurement of the vector and the tensor analyzing powers for the d-p elastic scattering at 270 MeV

In this chapter the experimental procedure and technique for the analyzing power measurement is presented. All components of the analyzing powers A_y, A_{yy}, A_{xx}, and A_{xz} for the d-p elastic scattering at $E_d^{\rm lab} = 270$ MeV have been measured for the angular range between 57° and 138°. The measurement was made by a kinematical coincidence method so that the ratio of the true events to accidental events was as good as a few hundred. This is the first measurement of a complete set of analyzing powers with high statistical precision at an intermediate energy. In the section 2.5, applicability of the d-p elastic scattering to a polarization analyzer of deuteron is considered.

2.1 RIKEN accelerator research facility

The measurement was performed at RIKEN accelerator research facility (RARF). This facility is particularly suited for the measurement of the deuteron polarization observables for the following reasons:

- The newly constructed polarized ion source provides a beam with large intensity and high polarization.

- The single-turn beam extraction is available both for the injector AVF cyclotron and the main RING cyclotron. This technique is crucial for maintaining the deuteron polarization during acceleration in the cyclotrons when the spin quantization axis is not parallel to the magnetic field of the cyclotrons.

Thus, RIKEN is a unique facility which provides a large intensity highly polarized deuteron beam whose spin quantization axis is freely controlled .

2.2 Polarized Ion Source

Block diagram of producing of the polarized deuteron beam is shown in Fig. 2.1. Molecular deuterium is dissociated by means of rf (radio frequency) induced discharge (**dissociator**). The atoms then pass through a nozzle which is cooled down to 35 K by a He refrigerator. An atomic beam with an appropriate emittance is selected by a skimmer from the atomic flow leaving the nozzle. Two **sextupole magnets** are used for focusing the atomic beam with the particular electron spin orientation, for example, "up" state component (see Fig. 2.1). The electron polarization is transferred to the nucleus by means of **rf transitions**. The nuclear polarized atomic beam is

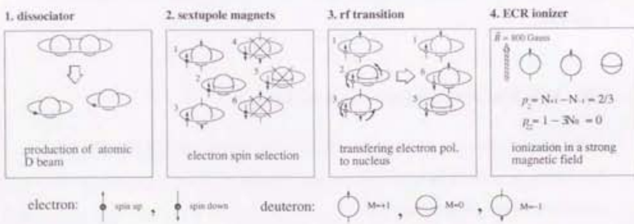

Figure 2.1: Block diagram of the production of polarized deuteron beam. The number 1~6 stands for the hfs substates number (see Appendix C). Here pure vector polarized deuteron beam ($p_Z = 2/3$, $p_{ZZ} = 0$) is obtained.

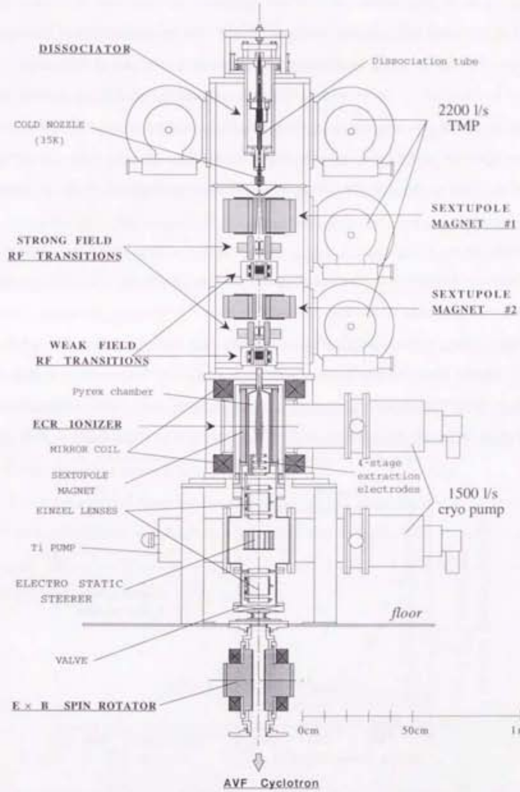

Figure 2.2: View of the RIKEN polarized ion source

ionized by an **ECR ionizer** under the axial magnetic field strength of about 1 kG and then extracted with a kinetic energy of 7.5 keV. The spin orientation of the beam is freely controlled by the Wien filter which is installed at the exit of the source.

A schematic view of the polarized ion source is shown in Fig. 2.2. The vertical design of the source provides a beam with longitudinal polarization which is convenient for the injection of the beam into the cyclotron without using an electro-magnetic deflector. Each element of the source is described in some detail in the following sections.

1. Dissociator

Molecular deuterium is dissociated into deuterium atoms by 13.56 MHz rf discharge in a Pyrex tube whose inner diameter is 8 mm. Dissociated deuterium atoms are cooled down by a cold nozzle which is placed at the exit of the dissociation tube.

The atomic beam intensities are shown as a function of the nozzle temperature in Fig. 2.3-(a). The intensity increases with the decrease of the nozzle temperature. However it decreases suddenly at 40 K. This temperature dependence is well un-

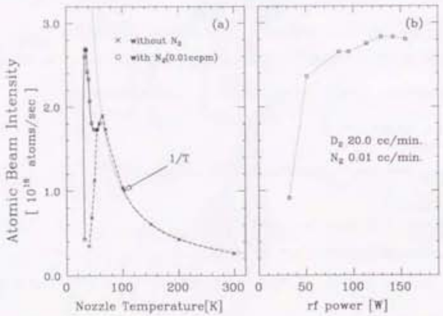

Figure 2.3: The atomic beam intensity as a function of the nozzle temperature (a) and the rf power (b)

derstood due to complete recombination of the atoms at the surface of the nozzle (indicated by the dashed curve). The temperature at which the intensity starts to decrease can be shifted to 30 K if a small amount of N_2 is added to the surface of the copper nozzle (indicated by the solid curve).

The atomic beam intensity as a function of the dissociator rf power is shown in Fig. 2.3-(b). The intensity saturates with the rf power of about 100 W. The S/N of the atomic beam, the ratio of the beam intensity with the sextupole magnets on to that with the sextupole magnet off, which has been measured at the exit of the injector AVF cyclotron depends on the amount of D_2 gas and was found to be maximized with the D_2 flow of 20 cc/min.

2. Sextupole magnets

In the sextupole magnetic field, the deuterium atoms with their electron spin up are separated from those with the electron spin down and are focused at the ionizer. The dimension of two sextupole magnets are summarized in Table. 2.2. In order to gain the focusing power, the first sextupole magnets was designed to have strong field at the entrance (see Appendix B).

Fig. 2.4 shows the atomic beam intensity for various magnetic field strength of the first sextupole magnet as a function of magnetic field strength of the second sextupole magnet. The atomic beam intensity seems to saturate with the pole tip field strength of 7 kG.

Table 2.1: Sextupole magnets

No.		aperture	length	pole tip field
		mmϕ	mm	kG (@250 A)
# 1	entrance	150	14	8.6
	exit		28	6.5
# 2		100	30	8.0

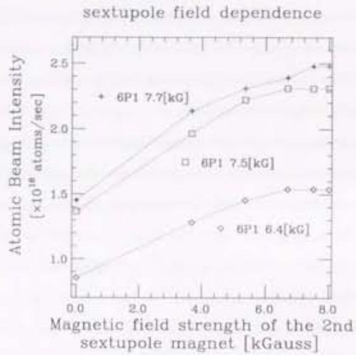

Figure 2.4: Atomic beam intensity via the pole tip field strength of the sextupole magnets

3. rf-transition

The state of polarization of nucleus is chosen by utilizing the adiabatic transitions between the hyper-fine-structure (hfs) states of the deuterium atom. Two kinds of the rf-transition units called as strong- and weak-field transition are located at the exit of each sextupole magnets (see Table. 2.2). With the combination of four transition units, any kind of vector and/or tensor polarizations can be produced.

Table 2.2: rf transition units.

rf units		rf frequency	transitions
SFT	# 1	330 MHz	3↔5
WFT	# 1	10 MHz	1↔4, 2↔3, and 5↔6
SFT	# 2	460 MHz	3↔5 (high field)
			2↔6 (low field)
WFT	# 3	10 MHz	1↔4, 2↔3, and 5↔6

The number 1∼6 stands for the hfs substates number.

4. Ionizer

Due to the high electron density of an ECR plasma a higher ionization efficiency is expected compared to an electron bombardment ionizer. Furthermore the space-charge-neutral ECR plasma enables us to extract a beam of small energy spread.

The ECR plasma is isolated from the ground potential by a Pyrex chamber and biased to +7.5 kV by the four-stage extraction electrodes. The ionized deuterium is extracted by the electric field gradient formed by the four-stage electrodes whose aperture is 5cmϕ. The degree of the polarization is largely depends on the background pressure in the ECR chamber. Two Ti sublimation pumps and one cryo pump are used to evacuate the ECR chamber through a large aperture of the extraction electrodes.

6. Wien filter

Schematic view of the spin control system at RIKEN is shown in Fig. 2.5-(b). The deuteron spin is rotated by a "$\vec{E} \times \vec{B}$" Wien filter, which is installed in the injection line to the AVF cyclotron, without bending the beam direction. Owing to the low energy of the beam (7.5 keV), the Wien filter is very compact. The single turn extraction is made for the cyclotrons so as not to reduce the polarization amplitude.

The spin orientation at the target point is obtained by using a polarimeter which can measure "left-right" and "up-down" asymmetries. In order to make the spin have appropriate angle at the target point, a certain Wien filter angle θ_{WF} is chosen from the θ_{WF} dependence of the horizontal vector component p_x. A typical θ_{WF} dependence p_x is shown in Fig. 2.5-(a) and is fitted by a sine curve.

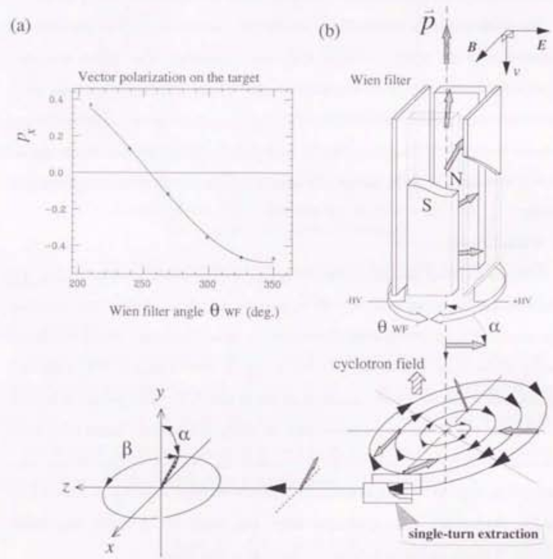

Figure 2.5: (a) Horizontal component of Vector polarization via the Wien filter angle θ_{WF}. (b) Schematic view of the RIKEN deuteron spin control system.

6. Operation

A typical set of the operation parameters is summarized in Table. 2.3

Table 2.3: Operation parameters of the polarized ion source

Dissociator			
rf power		100	W
D_2 gas flow		20.0	cc/min.
N_2 gas		0.01	cc/min.
Nozzle temp.		35.0	K
Sextupole magnets			
1st sextupole		250	A
2nd sextupole		250	A
ECR			
Mirror coil	# 1	111.2	A
	# 2	110.0	A
Micro wave		25.3–10.6	W
Buffer N_2		0.020	cc/min.
Extraction electrodes H.V.	# 1	7.5	kV
	# 2	7.4	kV
	# 3	5.0	kV
	# 4	gnd	
Vacuum			
Chamber	# 1	2.1×10^{-5}	Torr
	# 2	1.2×10^{-6}	Torr
	# 3	3.9×10^{-7}	Torr
	# 4	7.8×10^{-8}	Torr
	# 5	5.9×10^{-8}	Torr

3-Aug-1995, Cross section measurement

2.3 Calibration of the absolute value of the beam polarization

The vector and tensor polarized deuteron beams are at first accelerated up to 14 MeV by the injector AVF cyclotron and then up to 270 MeV by the main RING cyclotron. The absolute values of the beam polarizations, vector and tensor components, have been calibrated by using the $^{12}C(d,p)^{13}C_{gnd}$ reaction at $E_d^{lab} = 14$ MeV. The energy of 14 MeV corresponds to the injection energy of the main Ring cyclotron. The analyzing powers for the $^{12}C(d,p)^{13}C_{gnd}$ reaction at $E_d^{lab} = 14$ MeV have been measured (see Appendix D) in advance by using the well calibrated polarized deuteron beam at the Tandem van de Graaf accelerator of Kyushu University [19].

At $E_d^{lab} = 270$ MeV, the polarization monitor system makes use of the analyzing powers A_y and A_{yy} of the d-p elastic scattering. The analyzing powers of the analyzer have been determined as

$$A_y = -0.391 \pm 0.007 \quad \text{and} \quad A_{yy} = 0.478 \pm 0.016 \ , \tag{2.1}$$

where the errors are statistical ones only. Those values have been extracted under the assumption that the deuteron polarization was maintained and stable during the acceleration. This assumption can be justified as follows. The beam polarization was stable during this calibration procedure which was completed in a few hours is small. Typical vector and tensor polarizations are plotted as a function of time in Fig. 2.6. The uncertainty from the instability of the polarization is estimated to be about 2%. One of the major mechanism of depolarization is spin resonances in the cyclotron betatron oscillations. The depolarization resonance in the cyclotron oscillations occurs on the condition of

$$\gamma \cdot G = n \quad (\text{integer}) \ , \tag{2.2}$$

where $\gamma = (1 - \beta^2)^{-1/2}$ and G is anomalous magnetic moment. In the case of the deuteron the lowest kinetic energy which fulfill the resonance condition is 1.2 GeV so

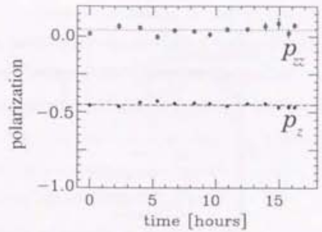

Figure 2.6: Time dependence of the beam polarization. The ideal values for vector and tensor polarizations are -2/3 and 0, respectively

that no depolarization resonance is passed through during the acceleration up to 270 MeV. Furthermore, the anomalous magnetic moment of the deuteron is so small that a partial depolarization arising from the spatial dispersion of the beam is expected to be negligible. At Saturne [20] and Dubna [21], the normalization for the absolute values of the proton and deuteron polarizations has been done based on the same assumption.

Although the method to derive the A_y and A_{yy} values of the polarization analyzer is quite reliable, it is important to measure the absolute values of the deuteron polarizations directly. We are preparing to measure the absolute values of the vector and tensor polarizations of the deuteron beam at $E_d^{lab} = 200$ MeV by using a unique reaction whose spin structure is $0^+ + 1^+ \rightarrow 0^+ + 0^-$. Details are described in Appendix H.

2.4 Experimental procedure

The measurement for the d-p elastic scattering at $E_d^{lab} = 270$ MeV was made by using a scattering chamber at the position (a) shown in the Fig. 2.7 in the experimental

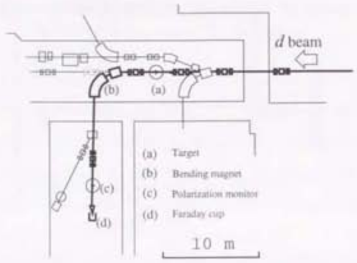

Figure 2.7: View of the experimental hall (analyzing power measurement)

hall D. As shown in Fig. 2.7, deuteron beams of the kinetic energy of 270 MeV came from right side along the solid line and bombarded the CH_2 target at the position (a). After bombarding the target, the beam was bent about 90° by the bending magnet (b) and was transported to the polarization monitor (c) in the experimental hall E3. The beam charge was collected by the Faraday cup (d) which was located about 2 meters downstream of the polarization monitor (c). The top and side views of the scattering chamber (a) are shown in Fig.2.8. In order to measure the d-p elastic scattering in four directions of left, right, up, and down, the chamber has four exit windows whose opening angles are ranging from 12° to 70° in the horizontal plane and from 12° to 60° in the vertical plane. Four pairs of detectors for kinematical coincidence detection of deuteron and proton were placed symmetrically in four directions, left, right, up, and down. Schematic view of one pair of the detectors are shown in Fig. 2.9. Each detector consisted of an NE102A plastic scintillator with a thickness of 1 cm coupled to an H1161 photo-multiplier tube. An aluminum block was placed in front of the plastic scintillator[1] to degrade the kinetic energy of the scattered particles such that

[1] In the degrader material, absorption of the charged particles is taken place. Since the absorption does not depend on the state of the polarization of deuteron or proton, the correction due to the orientation of polarization is not necessary in the analysis. (continued to next page)

their energy loss in the plastic scintillator was maximized. The block diagram of the electronics is shown in Fig. 2.10. The data were taken for coincidence trigger events generated by the signals of the proton counter and the deuteron counter in an interval of ±100 ns. The interval ±100 ns, which is larger than the interval of the bunched beams of the cyclotron, was chosen so as to obtain the accidentally coincidences. The dead time of the data acquisition was obtained by counting the number of the triggered events and the number of the accepted events.

The deuteron beams of intensity of 10–30 nA bombarded a polyethylene (CH_2) target with a thickness of 8.1 mg/cm². The detection of the scattered deuterons and recoil protons in a kinematic coincidence was essential to discriminate the d-p elastic scattering from other scattering processes such as the elastic scattering from carbon or the deuteron break-up process.

Since the mass of the incident particle is heavier than that of the target nucleus, the scattered particles are confined to forward angles and their energy varies quite rapidly with the increase of the scattering angle. The relations between the laboratory scattering angles θ_p (θ_d) and the scattering angle in the center of mass system $\theta_{c.m.}$, are shown in Fig. 2.11. An appropriate thickness of the aluminum degrader was chosen depending on the scattering angles. Scattering angles in the center of mass system $\theta_{c.m.}$ were determined by the angles of recoil protons θ_p. The opening angle of the proton detector $\Delta\theta_p$ was ±1.14°. The deuteron detector was designed to be large enough to cover the solid angle determined by the proton detector. Beyond $\theta_p = 60°$, the kinetic energy of the recoil proton becomes too small to detect and consequently

The absorption occurs through the interaction with aluminum nuclei. The total cross section of the reaction is independent from the vector polarization so that there is no effect arising from the vector polarization of deuterons or protons. However, the total cross section, in general, depends on the tensor polarization of deuterons t_{20}. Even under condition, the correction is not needed since the tensor analyzing power T_{20} is expected to be zero. This is because the main process of the deuteron absorption is due to the Coulomb break up process which is independent of the deuteron polarizations. In fact, the tensor analyzing power T_{20} of the deuteron break up with aluminum target has been measured at $E_d^{lab} = 56$ MeV and is found to be zero [22].

In the cross section measurement, the aluminum energy degraders were not employed.

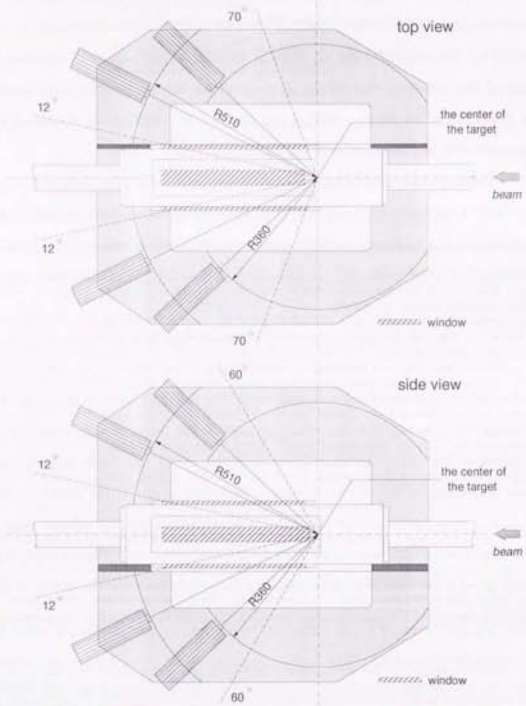

Figure 2.8: Top and side views of the scattering chamber

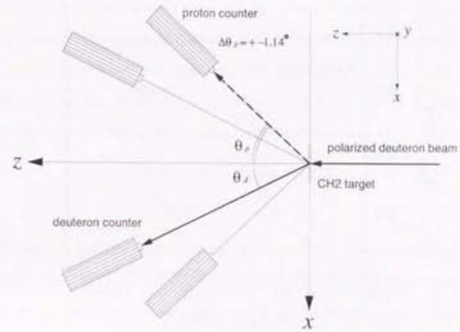

Figure 2.9: Schematic view of the counters setup for kinematical coincidence detection

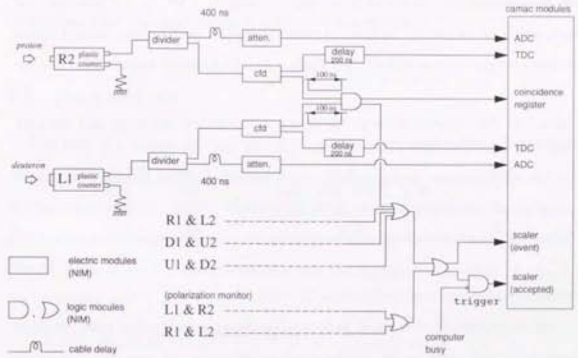

Figure 2.10: Schematic diagram of the trigger logic circuit

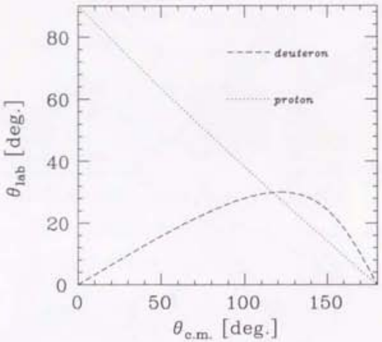

Figure 2.11: Kinematics of the d-p elastic scattering. (Angle in laboratory system vs. angle in center of mass system)

the measurement was restricted to the angular range $\theta_p \leq 60^\circ$ for left and right and $\theta_p \leq 60^\circ$ for up and down. In order to measure angular distributions, three different detector setups were employed (see Table 2.4). Consistency between the counter

Table 2.4: The distances between the proton detectors and the target and the solid angles of the proton detectors

set	θ_p	l_p(mm)	$\Delta\Omega_p$(msr)
I	20.0°, 25.0°, 35.0°, 40.0°	500	2.83
II	40.0°, 43.3°, 45.0°, 50.0°, 55.0°, 60.0°	350	2.79
III	30.0°	500	3.15

systems I and II has been confirmed at $\theta_p = 40^\circ$.

For the special case in which the outgoing deuteron and proton have the same laboratory angle of nearly 30°, the d-p elastic scattering in the directions of the both of left and right (up and down) was measured by one pairs of detectors. The two particles, protons and deuterons, could be clearly distinguished by their different

energy losses in the plastic scintillator and the differences between their time of flight from the target. The details of the data analysis are described in the next section.

The data were taken with polarized and unpolarized beams of the theoretical maximum values $(p_Z, p_{ZZ}) = (1/3, 1), (0, -2), (-2/3, 0)$, and $(0, 0)$, where p_Z and p_{ZZ} are vector and tensor polarizations, respectively, defined as

$$\begin{aligned} p_Z &= N_+ - N_- \,, \quad p_{ZZ} = 1 - 3N_0 \,, \\ \text{where} \quad & N_+ + N_0 + N_- = 1 \,, \end{aligned} \tag{2.3}$$

N_+, N_-, and N_0 are the occupation probabilities of the deuteron substates with the spin projections 1, -1, and 0, respectively. The polarization modes were changed cyclically at intervals of 20 seconds by switching the RF transition units of the ion source. The polarization monitor system, which was installed downstream of the target, also utilized the d-p elastic scattering at $\theta_{c.m.} = \pm 90^\circ$ as a polarization analyzer. The beam polarizations were monitored continuously and were found to be 60–70% of the theoretical maximum values throughout the experiment.

2.5 Data analysis

The analyzing powers A_y, A_{yy}, and A_{xx} were measured simultaneously with the deuteron spin normal to the horizontal plane. The analyzing powers are defined in the xyz frame of $\hat{z} \parallel \vec{k}_i$, $\hat{y} \parallel \vec{k}_i \times \vec{k}_f$, and $\hat{x} \parallel \hat{y} \times \hat{z}$, where $\vec{k}_i$ and $\vec{k}_f$ are the incident and scattered deuteron momenta, respectively. Following the Madison convention [23, 24], yields of the d-p elastic scattering with the deuteron polarization (p_Z, p_{ZZ}) can be written as

$$\begin{aligned} N_{\rm pol}(\theta,\phi) = n_{\rm pol}\frac{N_{\rm unpol}(\theta,\phi)}{n_{\rm unpol}}[1 &+ \frac{3}{2}p_Z A_y(\theta)\cos\phi \\ &+ \frac{1}{2}p_{ZZ}A_{xx}(\theta)\sin^2\phi \\ &+ \frac{1}{2}p_{ZZ}A_{yy}(\theta)\cos^2\phi] \,. \end{aligned} \tag{2.4}$$

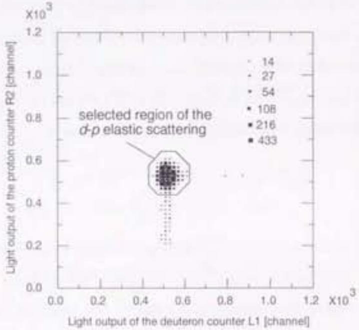

Figure 2.12: Spectrum of the light output of L1 vs. that of R2. The gate selects the region of the d-p elastic scattering.

Here N_{pol} and N_{unpol} are the yields with polarized and unpolarized beams respectively, n is the number of deuterons incident on the target, θ is the scattering angle, and ϕ is the azimuthal angle (with respect to the beam) between the normal to the scattering plane and the spin symmetry axis. The azimuthal angles ϕ for four pairs of detectors in the directions of left, right, up, and down are 0, π, $-\pi/2$, and $\pi/2$ radian, respectively.

The yield N is obtained by selecting events with the gate for the plastic scintillator light output of the deuteron counter and the proton counter (see Fig. 2.12) from the coincidence events which were taken by data taking system shown in Fig. 2.10. Accidental coincidence events which were obtained from the spectrum of the difference between the time of flight of the deuteron and that of the proton is corrected for.

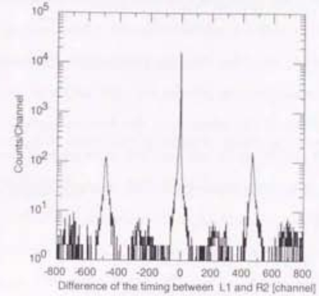

Figure 2.13: Spectrum of the difference of the time of flight between L1 and R2.

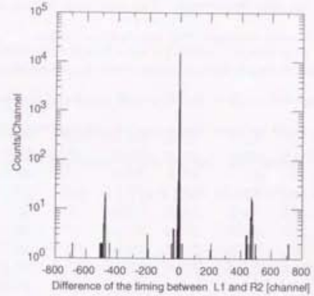

Figure 2.14: Spectrum of the difference of the time of flight between L1 and R2 for the selected events by the gate shown in Fig. 2.12.

In Fig. 2.13 and 2.14, the peak of the true timing events is located at the channel of zero and the peaks of the accidental coincidence events are located at the channel of $\pm$ 480. The difference of 480 channels corresponds to the intervals of the bunched beam from the cyclotron. Note that the peak count of the true events is not reduced by the selection. It implies that the gate for the light output of the counters was set appropriately. Correction of the efficiency of the data acquisition is obtained from the ratio between the number of "event" and that of "triggered" (see Fig. 2.10).

From Eq. (2), by using normalized yields $N'(\theta,\phi) = \frac{N_{pol}(\theta,\phi)/n_{pol}}{N_{unpol}(\theta,\phi)/n_{unpol}}$, A_y, A_{yy}, and A_{xx} were extracted as

$$
\begin{aligned}
A_y(\theta) &= \frac{N'(\theta,0) - N'(\theta,\pi)}{3p_Z}, \\
A_{yy}(\theta) &= \frac{N'(\theta,0) + N'(\theta,\pi) - 2}{p_{ZZ}}, \\
A_{xx}(\theta) &= \frac{N'(\theta,-\pi/2) + N'(\theta,\pi/2) - 2}{p_{ZZ}}.
\end{aligned}
\tag{2.5}
$$

This method does not require an accurate knowledge of the detector geometries and/or efficiencies of the detection system. The analyzing powers A_y, A_{yy}, and A_{xx} extracted by Eqs. (2.5) were averaged over polarization modes.

In the measurement of the tensor analyzing power A_{xz}, the spin symmetry axis of the deuteron beam was rotated into the horizontal plane and inclined to β = 142.2° $\pm$ 0.7° where β is the angle between the beam direction and the spin symmetry axis by using a Wien filter system [26]. The d-p elastic scattering yields for $\phi = \pi/2$ and $-\pi/2$ (left and right) are written by using β as

$$
\begin{aligned}
N_{pol}(\theta,\mp\pi/2) &= n_{pol}\frac{N_{unpol}(\theta,\mp\pi/2)}{n_{unpol}} \times \\
&\quad [\ 1 \pm \frac{1}{2} p_{ZZ} A_{xz}(\theta)\sin 2\beta + \frac{1}{2} p_{ZZ}(A_{xx}(\theta)\sin^2\beta + A_{zz}(\theta)\cos^2\beta)\ ].
\end{aligned}
\tag{2.6}
$$

A_{xz} can be extracted from these yields as

$$
A_{xz}(\theta) = \frac{N'(\theta,-\pi/2) - N'(\theta,\pi/2)}{p_{ZZ}\sin 2\beta}, \tag{2.7}
$$

and were averaged over the polarization modes.

2.6 Results of the analyzing power measurement

The measured vector and tensor analyzing powers A_y, A_{yy}, A_{xx}, and A_{xz} are listed in Table 2.5 and plotted via. the scattering angle in the center of mass system $\theta_{c.m.}$ in Fig. 2.15 with statistical errors. All the analyzing powers vary smoothly with the scattering angle $\theta_{c.m.}$. The vector analyzing power A_y crosses zero at $\theta_{c.m.}$ = 60° and 140°and have minimum at $\theta_{c.m.}$ = 100°. The tensor analyzing powers A_{yy}, A_{xz} have large positive values while A_{xx} have negative values in the angular range between 57° and 138°. The solid, dashed, dot-dashed lines in Fig. 2.15 are the theoretical predictions of the Faddeev

Table 2.5: Analyzing powers for the d-p elastic scattering at E_d^{lab} = 270 MeV

θ_p (deg.)	$\theta_{c.m.}$ (deg.)	A_y	ΔA_y	A_{yy}	ΔA_{yy}	A_{xx}	ΔA_{xx}	A_{xz}	ΔA_{xz}
20.0	137.8	−0.046	0.006	+0.559	0.020	−0.285	0.014	0.656	0.150
25.0	127.3	−0.199	0.007	+0.600	0.011	−0.248	0.008	0.566	0.072
30.0	116.9	−0.302	0.019	+0.687	0.074	−0.326	0.043	0.581	0.093
35.0	106.7	−0.382	0.006	+0.612	0.018	−0.385	0.013	0.360	0.033
40.0	96.6	−0.400	0.005	+0.544	0.013	−0.438	0.011	0.463	0.043
43.3	90.0	−0.391	0.007	+0.478	0.016	−0.450	0.014	0.481	0.032
45.0	86.5	−0.381	0.006	+0.491	0.016	−0.492	0.014	0.377	0.038
50.0	76.6	−0.297	0.006	+0.382	0.015	−0.502	0.016	0.339	0.040
55.0	66.8	−0.164	0.004	+0.329	0.013	−0.500	0.015	0.311	0.039
60.0	57.0	+0.030	0.003	+0.314	0.010	–	–	0.152	2.4e−02

The errors are statistical ones only.

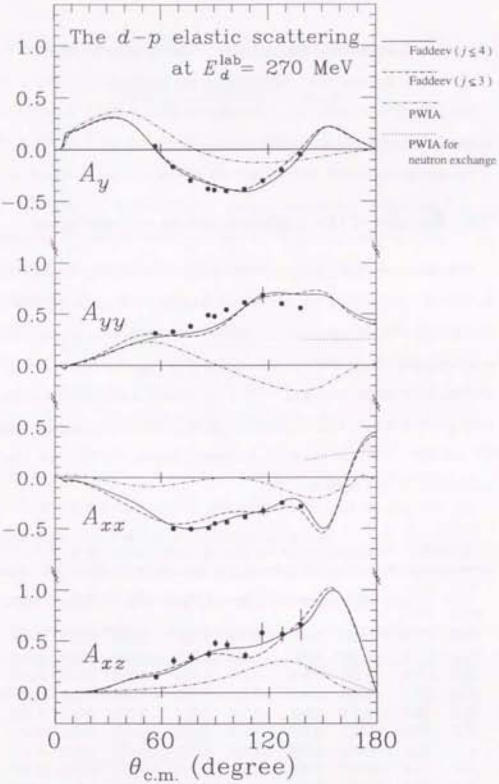

Figure 2.15: A_y, A_{yy}, A_{xx}, and A_{xz} for the d-p elastic scattering at $E_d^{\mathrm{lab}} = 270$ MeV. The solid, dashed, dot-dashed lines are theoretical predictions of the Faddeev calculation with the NN partial waves $j \leq 4$, and that with $j \leq 3$, and PWIA for direct elastic scattering process, respectively. Dotted lines are PWIA predictions for the neutron transfer reaction.

calculations with the NN partial waves $j \leq 4$, and with $j \leq 3$, and the predictions of PWIA for direct elastic scattering process, respectively. Details of the calculations are described in chapter 4 and 5.

The statistical errors are ± 0.006 or less for A_y, ± 0.02 or less for A_{yy} and A_{xx}, and $\pm 0.02 \sim \pm 0.15$ for A_{xz}. A rather large errors for A_{xz} is due to the fact that the sensitivity of A_{xz} to the tensor polarization p_{ZZ} is smaller by $\sin 2\beta$ than those of A_{yy} and A_{xx} (compare Eq. (2.7) with Eqs. (2.5)). There remain a systematic error $\pm 2\%$ from the uncertainty of A_y, and A_{yy} of the polarization analyzer. The tensor analyzing power A_{xz} has an additional uncertainty from the uncertainty of $\pm 2\%$ the spin angle β.

2.7 Application to a deuteron polarization analyzer

Finally, we would like to mention the applicability of the d-p elastic scattering as a polarization analyzer at intermediate energies. In general, the elastic scattering with carbon is utilized to measure a polarization of deuterons at intermediate energies. Although the elastic scattering with carbon has large vector analyzing powers with large cross sections, the tensor analyzing powers are very small. On the other hand, the d-p elastic scattering has following advantages as a polarization analyzer :

1. All components of the analyzing powers are large.
2. The angular distributions of the analyzing powers are smooth.
3. The clear event identification by a coincidence method is possible.

Therefore the d-p elastic scattering is suitable for the simultaneous measurement of vector and tensor components of deuteron polarization. There exist deuteron polarimeters which utilize the d-p elastic scattering. AHEAD [18] is dedicated to measure the tensor polarization t_{20} of scattered deuterons. DPOL [27], which has been constructed to measure polarization transfer coefficients for the deuteron inelastic scattering, was designed to measure all components of the scattered deuteron polarization simultaneously by utilizing the d-p elastic scattering as well as $^{12}C(d,d)$, and $^{1}H(d,2p)n$ reactions. At RIKEN, the d-p elastic scattering is also utilized to measure the beam polarization. It takes only 10 minutes to obtain the vector and tensor polarizations to a statistical accuracy of a few percent.

It should be noted that the tensor analyzing power A_{zz} $(= -(A_{yy} + A_{xx}))$ crosses zero at $\theta_{c.m.} = 86.6°$and consequently the beam intensity of the polarized beam can be obtained by the sum of the count-rates of left, right, up, and down at $\theta_{c.m.} = 86.6°$irrespective of the beam polarization. From Eq. (2.4) the sum of the left, right, up, and down yields are derived as

$$\begin{aligned} N_{pol}(\theta,0) \; + \; N_{pol}(\theta,\pi) \; + \; N_{pol}(\theta,-\pi/2) \; + N_{pol}(\theta,\pi/2) \\ = \; n_{pol}\frac{N_{unpol}(\theta)}{n_{unpol}}\left[4-\frac{1}{2}p_{ZZ}\,A_{zz}\right]. \end{aligned} \qquad (2.8)$$

Therefore, at the angle where $A_{zz} = 0$, the sum of the left, right, up, and down yield is proportional to the number of incident particles n_{pol} irrespective of the beam polarization.

As is clear that the d-p elastic scattering is a convenient and reliable tool to analyze the deuteron polarizations. Therefore the d-p elastic scattering will be used extensively as a polarization analyzer at intermediate energies.

Chapter 3

Measurement of the differential cross sections for the d-p elastic scattering at 270 MeV

The measurement of the differential cross sections were made separately to improve an accuracy in the absolute values. The beam transport downstream the target was changed to minimize the loss of the beam current between the target and the Faraday cup. In the case of the analyzing power measurement, the beam was transported to the polarization monitor after bombarding the target. In this arrangement, the loss of the beam charge was expected at the bending magnet (b) (see Fig. 2.7) which has a small aperture. The new arrangement has made an accurate measurement of the beam charge possible.

3.1 Measurement and result

The differential cross sections were measured with unpolarized deuteron beam with a polyethylene film target whose thickness was 40.5 ± 0.8 mg/cm^2. The size of multiple scattering of the beam by the target is estimated to be $\pm0.04°$. The beam intensity was 1~3 nA. Note that the thickness of the target was not changed by bombarding the beam. The yield at $\theta_p = 20°$ which was measured at the beginning of this experiment agrees with the yield at $\theta_p = 20°$ measured at the end of the experiment within the statistical error. The diameter of the beam spot on the target was less than 2 mm. The experimental setup was basically the same as in the analyzing power

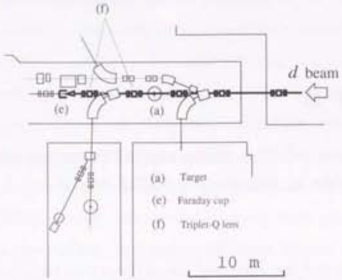

Figure 3.1: View of the experimental hall (cross section measurement)

measurement

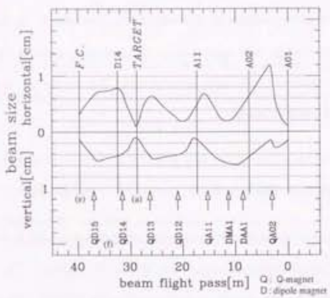

Figure 3.2: Beam envelope for the cross section measurement.

except for the following points to retain the accuracy:

1. The counters of up and down were not used in the cross section measurement.
2. Aluminum degraders were not used in the cross section measurement to avoid the loss of deuteron and proton flux by interactions in the degrader material.
3. After bombarding the target, the beam was transported by two triplet Q-lenses to the new Faraday cup which was about 10 meters downstream the target along the straight line.

It should be noted that the effective solid angle of the Faraday cup (f) is 0.7×10^{-3} sr so that the number of particles which are scattered into the Faraday cup is negligibly small. The differential cross sections are listed in Table 3.1 and plotted in Fig. 3.3. The solid, dashed, and dot-dashed lines are the same as in Fig. 2.15. The statistical uncertainties, which are smaller than the size of the solid circle symbols, are within ±1% for all angles. The measured yields of left and right counters agreed within ±3%, which implies the error arising from a geometrical misalignment of the

Table 3.1: Differential cross sections for the d-p elastic scattering at $E_d^{\rm lab} = 270$ MeV

θ_p [deg.]	$\theta_{c.m.}$ [deg.]	$d\sigma/d\Omega_{c.m.}$ [mb/sr]	$\Delta d\sigma/d\Omega_{c.m.}$ [mb/sr]
20.0	137.8	0.233	0.003
25.0	127.3	0.227	0.002
30.0	116.9	0.228	0.004
35.0	106.7	0.240	0.003
40.0	96.6	0.288	0.005
43.3	90.0	0.357	0.003
45.0	86.5	0.401	0.003
50.0	76.6	0.541	0.004
55.0	66.8	0.766	0.006
60.0	57.0	1.088	0.011

The errors are statistical ones only.

Table 3.2: Systematic errors for the differential cross sections

Origins of systematic errors	error
Target thickness	±2%
Detection efficiency	±3%
Charge collection	±5%

counters, efficiencies of the data taking system, and background subtraction, is estimated to be within ±3%. There remains a systematic error due to incomplete charge collection of the beam. The calculated beam envelope of the present measurement is shown in Fig. 3.2. The maximum size of the beam downstream the target is less than 2 cm in diameter which is much smaller than the size of the beam tube of 6 cm in diameter. Therefore the beam charge was collected by the Faraday cup without any loss. However, in practice, the efficiency of the collection depends on the condition of the beam transport which is largely affected by the cyclotron condition. Based on several experiences, we estimate the size of the systematic error by the incomplete charge collection less than ±5%. The total uncertainties in the final cross section are statistical error of ±1% and systematic errors of ±2% (target thickness) ±3% (detection efficiency) ±5% (beam charge).

3.2 Effect of carbon in the polyethylene target

It should be noted that the proton knock-out reaction from the carbon contained in the polyethylene target might influence the result of the d-p elastic scattering measurement since some of the final products in some cases such as the knock-out reaction $^{12}C(d,dp)^{11}B$ are indistinguishable from those of the d-p elastic scattering. We have measured coincidence yields of deuterons and protons with a carbon target at an angle corresponding to $\theta_{c.m.} = 86.6°$ of the d-p elastic scattering. It is found that the contribution of the $^{12}C(d,dp)^{11}B$ knock-out reaction to the measured d-p elastic

scattering is found to be less than 1% . The size of the contribution to the analyzing powers is also found to be less than 1% .

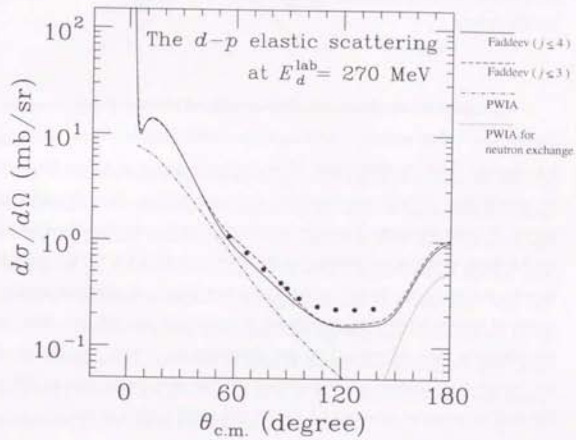

Figure 3.3: Differential cross sections for the d-p elastic scattering at E_d^{lab} = 270 MeV. The solid, dashed, dot-dashed lines are the same as in 2.15

Chapter 4

Impulse approximation for the d-p elastic scattering

In this chapter the d-p elastic scattering is considered in terms of impulse approximation model where one of the nucleons in the deuteron makes a single scattering with proton. Since the wave length of the incident deuteron at $E_d^{\mathrm{lab}} = 270$ MeV becomes as small as the size of the nucleon, it is expected that the single scattering process becomes dominant. The basic formalism of the impulse approximation for the d-p elastic scattering is introduced in the following sections 4.1, 4.2, 4.3, and 4.4. In order to simplify the calculation of the scattering matrix, an additional approximation of optimal factorization is made and described in section 4.2. In section 4.5, the differential cross sections and the spin observables are derived. Comparisons of the impulse approximation model prediction with the experimental data at $E_d^{\mathrm{lab}} = 270$ MeV are presented in section 4.6 and discussions are made in section 4.7.

4.1 Scattering matrix

An impulse approximation formalism for the d-p elastic scattering is derived following the basic idea of the PWIA for the (d, ^{2}He) reaction which is introduced by Bugg and Wilkin [28]. The following approximations are made; The effects arising from multiple scattering are neglected; The D-state component of the deuteron wave function is not included; Non-relativistic treatment is made; Exchange process is not

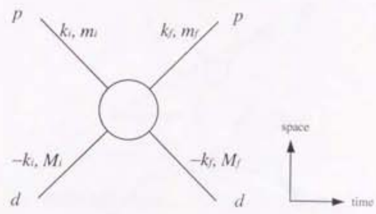

Figure 4.1: Scattering diagram for the d-p elastic scattering

considered.

Fig. 4.1 shows a scattering diagram for the d-p elastic scattering in the center of mass system. In the diagram, time-axis and spatial axis are taken along horizontal (left to right) line and vertical (down to up) line, respectively [29]. The initial and final state of the d-p elastic scattering are described by the deuteron internal wave function ψ^M with spin projection M, the proton internal wave function ϕ^m with spin projection m, and the deuteron-proton wave function with relative momentum $2\vec{k}$. In impulse approximation, one of the nucleons in the deuteron undergoes a single scattering with proton as shown in Fig. 4.2 where $\vec{p}$ is the deuteron internal momentum. The impulse-approximation amplitude is represented as

$$\hat{F}(\vec{q}; M_i, M_f, m_i, m_f) = \sum_{j=1}^{2} \langle \psi_f^{M_f}, \phi_f^{m_f} | f_{j3}^{NN} \exp(-\frac{i}{2}\vec{q}\cdot\vec{r}) | \psi_i^{M_i}, \phi_i^{m_i} \rangle \tag{4.1}$$

The argument $\vec{r}$ is the relative position between two nucleons in the deuteron. f_{j3}^{NN} is the NN scattering amplitude between the j-th [1] nucleon in the deuteron and the proton. In calculating this amplitude the f^{NN} should be integrated over the deuteron internal momentum $\vec{p}$. To simplify the calculation, the optimal factorization

[1] 1: proton in the deuteron, 2: neutron in the deuteron, 3: target proton

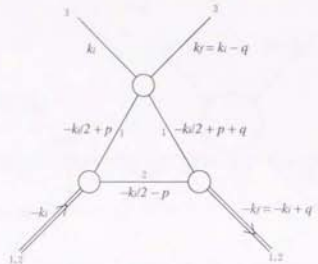

Figure 4.2: Scheme of the single scattering process

approximation is introduced. Since f^{NN} varies slowly with the target momentum(on the deuteron scale), it is permissible to take it out of the integration at some optimal value of $\vec{p_o}$. Then the amplitude can be represented by the product of the deuteron form factor $As(\vec{q})$ and spin scattering matrix Z;

$$F = As(\vec{q}) \cdot Z \quad . \tag{4.2}$$

The form factor of the deuteron is;

$$As(\vec{q}) = \int \psi_S^*(\vec{r}) \exp(\frac{i}{2}\vec{q} \cdot \vec{r}) \psi_S(\vec{r}) d^3 r \tag{4.3}$$

and Z represents the spin part;

$$Z = \sum_{j=1}^{2} \langle \chi_m^p | \langle \chi_M^d | \langle \vec{k_i} - \vec{q}, -\frac{1}{2}\vec{k_i} + \vec{p_o} + \vec{q} | f_{j3}^{NN} | \vec{k_i}, -\frac{1}{2}\vec{k_i} + \vec{p_o} \rangle | \chi_M^d \rangle | \chi_m^p \rangle \ . \tag{4.4}$$

The NN amplitude f_{j3}^{NN}, e.g. neutron-proton and proton-proton scattering amplitudes, are given as a function of θ_{NN} and scattering energy T_{NN} in the convention of KMT (Kerman–McManus–Thaler) notation [30] by

$$f_{j3}^{NN}(T,\theta) = A + C(\sigma_j \cdot \hat{n} + \sigma_3 \cdot \hat{n}) + B(\sigma_j \cdot \hat{n})\,(\sigma_3 \cdot \hat{n}) + E(\sigma_j \cdot \hat{q})\,(\sigma_3 \cdot \hat{q}) + F(\sigma_j \cdot \hat{p})\,(\sigma_3 \cdot \hat{p}). \tag{4.5}$$

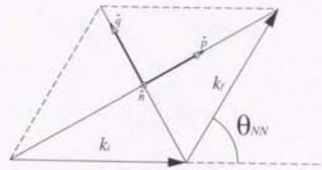

Figure 4.3: $\hat{n}\hat{q}\hat{p}$ frame for the NN scattering

with the unit vectors $\hat{n}$,$\hat{q}$, $\hat{p}$ which are defined by the initial momentum $\vec{k_i}$ and the final momentum $\vec{k_f}$.

$$\hat{n} = \frac{\vec{k_i} \times \vec{k_f}}{|\vec{k_i} \times \vec{k_f}|}, \quad \hat{q} = \frac{\vec{k_f} - \vec{k_i}}{|\vec{k_f} - \vec{k_i}|}, \quad \hat{p} = \hat{q} \times \hat{n} \tag{4.6}$$

The parameters T_{NN}, $\vec{q}$ and the initial and final momenta $\vec{k_i}$, $\vec{k_f}$ are related through

$$\vec{q} = \vec{k_i} - \vec{k_f} \ \text{ and } \ T_{NN} = \sqrt{|\vec{k_i}|^2 + {m_N}^2} - m_N. \tag{4.7}$$

Note that, since the effect of the Coulomb force is included in the proton-proton scattering amplitude, the effect of the Coulomb force between deuteron and proton is automatically taken into account in the calculation with the form of Born approximation.

4.2 Optimal factorization

The single scattering diagram in the deuteron Breit frame (or Brick Wall system) [31] is shown in Fig. 4.4. In this frame the most appropriate choice of the optimal momentum is $\vec{P} = 0$ [32]. The choice of the optimal momentum $\vec{P} = 0$ results the 1-3 scattering itself in the NN Breit frame (Fig. 4.5) on the on-energy-shell condition in NN scattering. The choice of the optimal momentum in the deuteron Breit frame $\vec{P_o}$ as zero implies that the optimal internal momentum is $-\frac{1}{4}\vec{q}$ in the Breit frame.

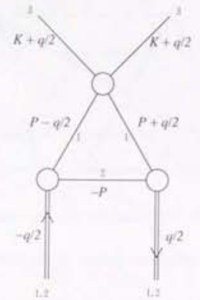

Figure 4.4: Deuteron-proton scattering diagram in deuteron Breit frame

i.e., the optimal internal momentum in the d-p center of mass frame $\vec{p}_o$ is $-\frac{3}{4}\vec{q}$. The NN scattering amplitudes of Eq. 4.5 are obtained from the nucleon-nucleon scattering phase shift analysis code SAID(SP94) [33].

4.3 Spin part of the scattering matrix

The NN amplitudes for the diagram shown in Fig. 4.5 corresponds to the amplitudes of scattering angle θ_{NN} and kinetic energy T_{NN} as;

$$\begin{aligned} \theta_{NN} &= \cos^{-1}\frac{\left(\frac{1}{2}\vec{K}+\frac{1}{2}\vec{q}\right)\cdot\left(\frac{1}{2}\vec{K}-\frac{1}{2}\vec{q}\right)}{|\frac{1}{2}\vec{K}+\frac{1}{2}\vec{q}||\frac{1}{2}\vec{K}-\frac{1}{2}\vec{q}|} = \cos^{-1}\frac{|\vec{K}|^2-|\vec{q}|^2}{|\vec{K}|^2+|\vec{q}|^2} \\ T_{NN} &= \frac{1}{2m}(|\vec{K}+\vec{q}|^2) = \frac{1}{2m}(|\vec{K}|^2+|\vec{q}|^2) \quad , \end{aligned} \tag{4.8}$$

and averaged over the nucleon number in deuteron, i.e. the amplitudes are averaged over the neutron-proton and the proton-proton channels.

The spin part of the deuteron wave function $|\chi_M^d\rangle$ can be written by using proton

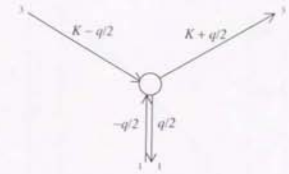

Figure 4.5: Scattering diagram between the target proton and one of the nucleons in deuteron

and neutron spins as

$$\begin{aligned} |\chi_M\rangle_d &= \sum_{m_1,m_2=\pm\frac{1}{2}} \langle 1M|\,\frac{1}{2}\,m_1\,\frac{1}{2}\,m_2\rangle \\ &= \sum_{m_1,m_2=\pm\frac{1}{2}} T^{12}|\chi_{m_1}\rangle_p|\chi_{m_2}\rangle_n \quad , \end{aligned} \tag{4.9}$$

where T^{12} is a spin projection operator (see Appendix G) for $S_d = 1$ triplet state represented as

$$T^{12} = \frac{1}{4}\left(3+\vec{\sigma}^1\cdot\vec{\sigma}^2\right) \tag{4.10}$$

Spin operator Z is written as

$$\begin{aligned} Z &= K(\theta_{NN})\sum_{j=1,2}\sum_{m_1,m_2=\pm\frac{1}{2}} {}_p\langle\chi_{m_1}|_n\langle\chi_{m_2}|\,T^{12}\,[A_{j3}(\theta_{NN},T_{NN}) \\ &+ B_{j3}(\theta_{NN},T_{NN})\left(\vec{\sigma}^j\cdot\hat{n}+\vec{\sigma}^3\cdot\hat{n}\right) \\ &+ C_{j3}(\theta_{NN},T_{NN})\left(\vec{\sigma}^j\cdot\hat{n}\right)\left(\vec{\sigma}^3\cdot\hat{n}\right) \\ &+ E_{j3}(\theta_{NN},T_{NN})\left(\vec{\sigma}^j\cdot\hat{q}\right)\left(\vec{\sigma}^3\cdot\hat{q}\right) \\ &+ F_{j3}(\theta_{NN},T_{NN})\left(\vec{\sigma}^j\cdot\hat{p}\right)\left(\vec{\sigma}^3\cdot\hat{p}\right)]\,T^{12}\,|\chi_{m_1}\rangle_p|\chi_{m_2}\rangle_n \quad . \end{aligned} \tag{4.11}$$

$K(\theta_{NN})$ is a kinematical factor defined as

$$K(\theta_{NN}) = \frac{\sin\theta_{NN}\,d\theta_{NN}}{\sin\theta_{c.m.}\,d\theta_{c.m.}} \quad , \tag{4.12}$$

which is required because the NN amplitudes are given in the NN center of mass system. It is also needed to translate the spin part to that in the deuteron-proton

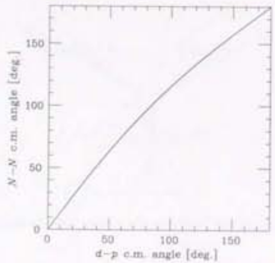

Figure 4.6: Kinematics for the optimal factorization approximation

center of mass system, though it is neglected here since the difference between θ_{NN} and $\theta_{c.m.}$ is as small as a few degrees.

4.4 Form factor

The from factor

$$A_S(\vec{q}) = \int \phi_S^*(\vec{r}) e^{i\vec{q}\cdot\vec{r}/2} \phi_S(\vec{r}) d\vec{r} \tag{4.13}$$

can be analytically integrated over angular part θ, and ϕ as

$$A_S(\vec{q}) = 4\pi \int |\phi_S|^2 \frac{\sin qr/2}{qr/2} r^2 dr \ . \tag{4.14}$$

By using this form the form factor was numerically integrated over radial part r. In the calculation a parameterized deuteron wave function (Appendix F) is used.

$$\phi_S(r) = \frac{U(r)}{r} Y_0^0 \chi_1^1 = \sqrt{\frac{1}{4\pi}} \sum_{i=1}^{13} C_i \frac{\exp(-m_i r)}{r} \ . \tag{4.15}$$

The form factor vs. transferred momentum q is shown in Fig. 4.7.

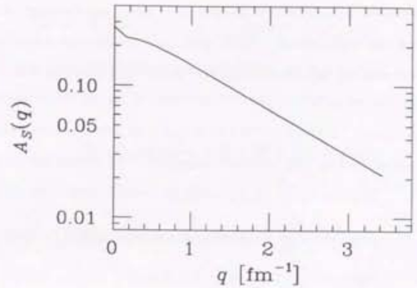

Figure 4.7: Form factor $A_S(q)$

4.5 Observables

Making an optimal factorization approximation, the scattering matrix for the d-p elastic scattering is represented as

$$F = A_S \cdot Z; , \tag{4.16}$$

where A_S is a form factor and Z is a spin scattering matrix. From the scattering matrix, the differential cross section is obtained as follows:

$$\begin{aligned} \frac{d\sigma}{d\Omega_{c.m.}} &= \mathrm{Tr}\left[FF^+\right] \\ &= A_S{}^2\, \mathrm{Tr}\left[ZZ^+\right] \end{aligned} \tag{4.17}$$

The spin observables of spin operator $\hat{S}$ are

$$\begin{aligned} \langle \hat{S} \rangle &= \frac{\mathrm{Tr}\left[F\hat{S}F^+\right]}{\mathrm{Tr}\left[FF^+\right]} = \frac{\mathrm{Tr}\left[Z\hat{S}Z^+\right]}{\mathrm{Tr}\left[ZZ^+\right]} \\ &= \sum_{m_1,m_2,m_3=\pm\frac{1}{2}} \langle m_1, m_2, m_3 | T^{12}\, \hat{S}\, T^{12+} | m_1, m_2, m_3 \rangle \\ &\quad / \sum_{m_1,m_2,m_3=\pm\frac{1}{2}} \langle m_1, m_2, m_3 | T^{12}\, T^{12+} | m_1, m_2, m_3 \rangle \end{aligned} \tag{4.18}$$

The spin observables are independent from the form factor and the kinematical factor. The vector and tensor spin operators in the spherical coordinate are defined in terms of the spin operators of the individual nucleons $\vec{\sigma}^1$ and $\vec{\sigma}^2$ and total spin $S = \frac{1}{2}\left(\vec{\sigma}^1 + \vec{\sigma}^2\right)$ by

$$\begin{aligned}
\Omega_{20} &= \frac{1}{\sqrt{2}}\left(3S_z^2 - 2\right) = \frac{1}{2\sqrt{2}}\left(3\sigma_z^1\sigma_z^2 - 1\right) && (4.19)\\
\Omega_{2\pm1} &= \mp\frac{\sqrt{3}}{2}\left(S_\pm S_z + S_z S_\pm\right) \\
&= \mp\frac{\sqrt{3}}{4}\left(\sigma_x^1\sigma_z^2 + \sigma_z^1\sigma_x^2 \pm i\sigma_y^1\sigma_z^2 + \pm i\sigma_y^1\sigma_z^2\right) && (4.20)\\
\Omega_{2\pm2} &= \frac{\sqrt{3}}{2}\left(S_\pm\right)^2 = \frac{\sqrt{3}}{2}\left(S_x \pm iS_y\right)^2 \\
&= \frac{\sqrt{3}}{4}\left(\sigma_x^1\sigma_x^2 - \sigma_y^1\sigma_y^2 \pm i\sigma_x^1\sigma_y^2 + \pm i\sigma_y^1\sigma_x^2\right) && (4.21)\\
\Omega_{10} &= \sqrt{\frac{3}{2}}S_z && (4.22)\\
\Omega_{1\pm1} &= -\frac{\sqrt{3}}{2}\left(S_x \pm iS_y\right) && (4.23)
\end{aligned}$$

The traces of bi-linear combinations of the spin operator Z are evaluated by using rules shown in appendix G and the observables are derived as follows:

$$\begin{aligned}
\langle ZZ^+\rangle &= 3|A|^2 + 5|C|^2 + 2|B|^2 + 2|E|^2 + 2|F|^2 && (4.24)\\
\langle Z\Omega_{20}Z^+\rangle &= -\frac{1}{\sqrt{2}}\left[|C|^2 + |B|^2 + |E|^2 - 2|F|^2\right] && (4.25)\\
\langle Z\Omega_{2\pm2}Z^+\rangle &= -\frac{\sqrt{3}}{2}\left[|C|^2 + |B|^2 - |E|^2\right] && (4.26)\\
\langle Z\Omega_{2\pm1}Z^+\rangle &= \langle Z\Omega_{10}Z^+\rangle = 0 && (4.27)\\
\langle Z\Omega_{1\pm1}Z^+\rangle &= \mp 2\sqrt{3}i\mathrm{Re}\left((A+B)^*C\right) && (4.28)
\end{aligned}$$

and the vector and tensor analyzing powers in spherical coordinate are

$$\begin{aligned}
T'_{20} &= -\frac{1}{\sqrt{2}}\left[\frac{|C|^2 + |B|^2 + |E|^2 - 2|F|^2}{3|A|^2 + 5|C|^2 + 2|B|^2 + 2|E|^2 + 2|F|^2}\right] && (4.29)\\
T'_{22} &= -\frac{\sqrt{3}}{2}\left[\frac{|C|^2 + |B|^2 - |E|^2}{3|A|^2 + 5|C|^2 + 2|B|^2 + 2|E|^2 + 2|F|^2}\right] && (4.30)\\
T'_{21} &= 0 && (4.31)
\end{aligned}$$

$$T'_{11} = \mp 2\sqrt{3}i\frac{\mathrm{Re}\left((A+B)^*C\right)}{3|A|^2 + 5|C|^2 + 2|B|^2 + 2|E|^2 + 2|F|^2} . \qquad (4.32)$$

The results have been obtained by quantizing along the $\hat{p}$ axis of Eq. (4.6) shown in Fig. 4.3. These variables can be converted into ones referring to quantization along the beam direction by using the standard transformations for tensor polarizations. Now the analyzing powers for the d-p elastic scattering by an impulse approximation with the deuteron S-wave function as follows:

$$T_{20} = \frac{1}{2}(3\cos^2\chi - 1)T'_{20} - \sqrt{6}\sin\chi\cos\chi\,\mathrm{Re}\,T'_{21} + \frac{\sqrt{3}}{\sqrt{2}}\sin^2\chi\,\mathrm{Re}\,T'_{22} \qquad (4.33)$$

$$T_{21} = (2\cos^2\chi - 1)\mathrm{Re}\,T'_{21} - \sin\chi\cos\chi(\mathrm{Re}\,T'_{22} - \frac{\sqrt{3}}{\sqrt{2}}T'_{20}) + i\cos\chi\,\mathrm{Im}\,T'_{21} - i\sin\chi\,\mathrm{Im}\,T'_{22} \qquad (4.34)$$

$$T_{22} = \frac{1}{2}(1 + \cos^2\chi)\mathrm{Re}\,T'_{22} + \sin\chi\cos\chi\,\mathrm{Re}\,T'21 + \frac{\sqrt{6}}{4}\sin^2\chi T'_{20} + i\cos\chi\,\mathrm{Im}\,T'_{22} + i\sin\mathrm{Im}\,T'_{21} \qquad (4.35)$$

where χ is the angle of rotation about $\hat{n}$ between the two frames (see Fig. 4.6) ;

$$\chi = \frac{1}{2}\theta_{NN} - (\theta_{c.m.} - \theta_{NN}) . \qquad (4.36)$$

The other observables in the spherical frame were translated to Cartesian frame through the following relations shown in appendix A. Though, A_y and A_{yy} are easily obtained from T' as

$$\begin{aligned}
A_y &= \frac{2}{\sqrt{3}}iT'_{11} \\
&= \frac{4\mathrm{Re}\left((A+B)^*C\right)}{3|A|^2 + 5|C|^2 + 2|B|^2 + 2|E|^2 + 2|F|^2} && (4.37)\\
A_{yy} &= -\sqrt{3}T_{22} - \frac{1}{\sqrt{2}}T_{20} \\
&= \frac{4\left(|C|^2 + |B|^2\right) - 2\left(|E|^2 + 2|F|^2\right)}{3|A|^2 + 5|C|^2 + 2|B|^2 + 2|E|^2 + 2|F|^2} . && (4.38)
\end{aligned}$$

4.6 Results of the PWIA calculations

The results of the PWIA calculations for the analyzing powers and the differential cross sections are shown by dot-dashed lines in Figs. 2.15 and 3.3 together with the experimental data.

The shape of the differential cross sections is reproduced by the PWIA calculation at forward angles ($\leq 90°$) reasonably well. The PWIA prediction falls off rapidly with the increase of the scattering angle beyond 90°, while the experimental data show minimum and constant values at the scattering angles between 100°and 140°. This rapid fall off is due to the behavior of the form factor $A_S(q)$ with the increase of the momentum transfer q (see Fig. 4.7).

Concerning with the analyzing powers of A_y and A_{xz}, their gross behaviors are roughly reproduced. The calculation does not reproduce the shape of the A_y at backward angles. While the experimental data of A_{yy} and A_{xx} have either positive or negative large values at angles between 57° and 138°, the predicted values are either crossing zero at 90° or almost zero.

Summarizing the comparison between the predictions of the present PWIA calculations and the data, the behaviors of the experimental data at the angles less than 90° are roughly reproduced for the differential cross sections and the analyzing powers A_y and A_{xz} by the calculation which is yet in a primitive stage. The tensor analyzing powers A_{yy} and A_{xx} are not reproduced. In order to improve the fit the inclusion of the effects which are neglected in the calculation might be needed.

4.7 Discussions

At this point it might be useful to review the effect which is neglected in the framework of the present PWIA calculation:

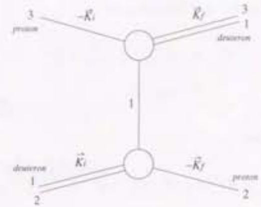

Figure 4.8: Diagram for the direct neutron exchange reaction

1. Neutron exchange process is not considered.

2. Deuteron D-state is neglected.

The neutron exchange process in which the neutron in the deuteron is transferred to the target proton forming a deuteron, might be dominant at backward angles since its form factor becomes maximum at 180°.

The deuteron D-state is, in general, important for the tensor analyzing powers. Although the inclusion of the deuteron D-state in the PWIA calculations is possible in principle, it is too involved because of a number of the terms. The deuteron wave function is composed of 6 terms and the NN scattering amplitude is composed of 5 terms so that the d-p scattering amplitude consists of $6\times5\times6 = 180$ terms. It is not at all simple any more loosing the merit of the simplicity of the PWIA treatment.

Therefore, we investigate the neutron exchange process which is still simple enough to handle hoping that the fit of the analyzing powers at backward angles will be improved.

The simplest neutron exchange process might be the one shown in Fig. 4.8. Similar to the PWIA calculation for elastic channel, the scattering amplitude F_{ex} for the diagram shown in Fig. 4.8 can be expressed as

$$\begin{aligned} F_{ex} &= \langle \phi^1_{m_f}, \psi^{23}_{M_f} | \phi^3_{m_i}, \psi^{12}_{M_i} \rangle \\ &= A_{ex} \cdot Z_{ex} \ . \end{aligned} \tag{4.39}$$

Here A_{ex} is the form factor;

$$A_{ex} = \langle \psi_d^{23*}(r_{23})\, V_{12}\, \psi_d^{12}(r_{12}) e^{i(\vec{K}_f \cdot \vec{R}_f + \vec{K}_i \cdot \vec{R}_i)} \rangle, \tag{4.40}$$

where $\vec{K}_i$, $\vec{K}_f$ are initial and final momenta, respectively and $\vec{R}$ is the relative position of the proton and the deuteron. The spin part of the scattering matrix Z is represented as:

$$\begin{aligned} Z_{ex} &= {}_p\langle \chi^2_{m_f} |\, {}_d\langle \chi^{13}_{M_f} | \chi^{23}_{M_i} \rangle_d | \chi^3_{m_i} \rangle_p \\ &= \langle \chi^1_{m_f} | \langle \chi^2_{m_f} | \langle \chi^3_{m_f} |\, T^{23} \cdot T^{12}\, | \chi^1_{m_i} \rangle | \chi^2_{m_i} \rangle | \chi^3_{m_i} \rangle \end{aligned} \tag{4.41}$$

The calculated differential cross sections and the analyzing powers are shown in Fig. 3.3 and Fig. 2.15, respectively, by the dotted curves for the angles between 140° and 180°. Note that the A_y is predicted to be zero in this model.

The differential cross sections are predicted to be large values at backward angles as expected, while those of the direct elastic process are almost zero. The behaviors of the analyzing powers differ from those of the direct elastic process. The predicted signs of A_{yy} and A_{xx} in this model are opposite to those in the direct process.

Inclusion of the neutron exchange process seems to improve the fit to the data. However there still remains a discrepancy in the differential cross sections at $\theta =$ 90°$\sim$ 140° where the cross sections have minimum values. It is certainly interesting how the prediction in PWIA can be improved by taking into account the interference between the direct and the exchange amplitudes as well as the deuteron D-state.

Chapter 5

Three-body calculation

In this chapter, the data are compared with the predictions of the three-body Faddeev calculation. The Faddeev theory describes few-body system exactly, in principle. In section 5.1, the basic idea of the Faddeev theory is described. In section 5.2, the outline of the three-body calculation for the d-p elastic scattering at $E_d^{lab} = 270$ MeV with a separable potential method is described [1]. The result of the three-body calculation is compared with the data in section 5.3 and discussions are made.

5.1 Faddeev theory

L. D. Faddeev has succeeded to describe a three-body system in terms of two-body scattering. Faddeev equation in a general form is written as;

$$\begin{pmatrix} T_{12} \\ T_{23} \\ T_{31} \end{pmatrix} = \begin{pmatrix} t_{12} \\ t_{23} \\ t_{31} \end{pmatrix} + \begin{pmatrix} 0 & t_{12} & t_{12} \\ t_{23} & 0 & t_{23} \\ t_{31} & t_{31} & 0 \end{pmatrix} \begin{pmatrix} T_{12} \\ T_{23} \\ T_{31} \end{pmatrix} , \tag{5.1}$$

where T_{ij} is the three-body scattering t-matrix, t_{ij} is a two-body NN scattering t-matrix which can be obtained by solving Lippman-Schwinger equation, and G_o is a Green function in a free space. From the Faddeev equation, it is easily understood that the three-body t-matrix can be represented in a form of expansion by two-body scattering t-matrix as;

$$T_{12} = t_{12} \ + \ t_{12}G_o t_{23} + t_{12}G_o t_{23}$$

[1] The Faddeev calculations presented in this thesis were made by Dr. Koike, *Hosei university*

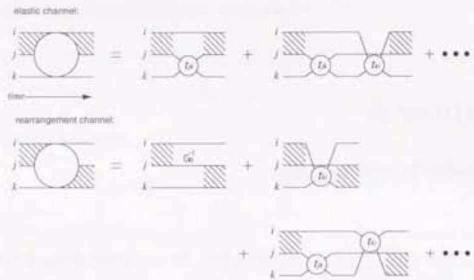

Figure 5.1: The first few terms in the multiple scattering series for elastic and rearrangement processes. The hatching represents that two nucleons are in bound.

$$\begin{aligned} &+ \; t_{12}G_{o}t_{23}G_{o}t_{12} \\ &+ \; t_{12}G_{o}t_{23}G_{o}t_{31} + \cdots \end{aligned} \tag{5.2}$$

In Fig. 5.1, the three-body scattering diagram expanded in terms of two-body scattering process is shown.

In the three-body calculation the multiple scattering process, rearrangement process (exchange), the contribution of off-the-energy-shell components of NN interactions, and the deuteron D-state are fully included.

5.2 Calculation for the d-p elastic scattering at $E_d^{\rm lab}$ = 270 MeV

A three-body calculation with a separable expansion method [34] was performed for the d-p elastic scattering at $E_d^{\rm lab} = 270$ MeV. Three-body force is not considered and the coordinates are treated non-relativistically. The d-p scattering t-matrix is approximated by a modified d-n scattering t-matrix which is corrected for the effect

of the Coulomb distortion in the manner of Ref. [35]. The d-n scattering t-matrix is obtained by solving the Faddeev equation with an NN interaction. The calculation was performed with the full two-body interactions for $j \leq 4$ involving 98 coupled channels for the scattering system. To solve the equation with a large number of coupled channels as in the present case, a separable expansion method is convenient. In the present calculation, the Argonne v_{14} potential [36] is employed and converted to a separable series by USE [37, 38]. The advantage of USE is that the separable series converges quickly. The ranks in the separable expansion used are shown in Table 5.1. By using a separable two-body t-matrix, two-dimensional integral Faddeev

Table 5.1: The ranks in the separable expansion of the Argonne v_{14} potential for $j \leq 3$ and $j = 4$

partial waves	$j \leq 3$										
	$^3s_1$-$^3d_1$	$^1s_0$	$^1p_1$	$^3p_0$	$^3p_1$	$^3p_2$-$^3f_2$	$^1d_2$	$^3d_2$	$^3d_3$-$^3g_3$	$^1f_3$	$^3f_3$
ranks	9	6	4	5	4	5	4	4	6	3	3

partial waves	$j = 4$		
	$^3f_4$-$^3h_4$	$^1g_4$	$^3g_4$
ranks	3	2	2

equations are reduced to coupled one-dimensional integral equations. The resulting one-dimensional coupled integral equations are converted to a matrix with 32-point Gaussian quadrature on a deformed contour. From the obtained matrix, a Born series is produced for the three-body on-shell scattering amplitude by using the Padé approximation which makes the Born series converge.

5.3 Comparison with the data and discussions

The results of the calculation with the NN interaction of $j \le 3$ and those of $j \le 4$ are shown in Fig. 2.15 and 3.3. Dashed and solid lines are the results of the calculation with $j \le 3$ and $j \le 4$, respectively. In Fig. 5.2, the difference between the calculation and the data is also shown. All components of the analyzing powers are found to be reproduced surprisingly well. The well-reproduction of the analyzing powers is notable because the fit of the calculation to the data is quite poor at low energies. Since the tensor analyzing power A_{xx}, which is known to be sensitive to the tensor part of the NN interaction at low energies, is described well, it might indicate that the tensor part of the Argonne v_{14} potential is determined adequately. Inclusion of the $j = 4$ wave slightly improves the fits of the calculated analyzing powers especially for A_{xx}. By Witala *et al.*, Faddeev calculations with $j \le 4$ have been performed at $E_d^{\rm lab} = 131$ MeV and 187 MeV [11]. They also reported that the inclusion of the $j =$ 4 higher partial wave only slightly changes the theoretical prediction with $j \le 3$.

In contrast, the fit to the differential cross sections is poor. The calculated cross sections are 30% smaller than the experimental values at angles around $\theta_{\rm c.m.} = 120°$ where the cross sections have a minimum (see Fig. 5.2). Inclusion of the $j = 4$ partial wave does not improve the prediction obtained with $j \le 3$.

The analyzing powers are ordinary thought to be much more difficult to be reproduced by calculation than the cross sections are so that it is surprising that the calculated cross sections are smaller by 30% than the data at the angles where the cross sections have minima while a good reproduction of the analyzing powers is obtained.

In order to see the energy dependence of the disagreement found in the differential cross sections, we have performed calculations with $j \le 3$ for deuteron incident energies of 130 MeV and 190 MeV and compared these with the existing experimental data [39, 40] in Fig. 5.4 together with the data at $E_d^{\rm lab}$= 270 MeV. Note that the differential

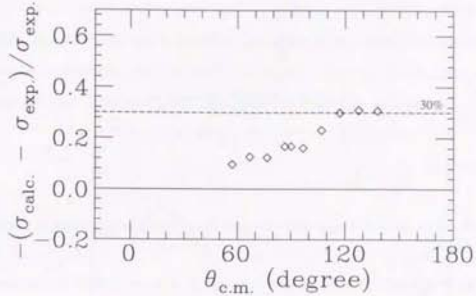

Figure 5.2: Difference of the calculation ($j \le 4$) and the data. The size of the discrepancy is 30% at $\theta_{\rm c.m.} = 117° \sim 138°$.

cross sections are not presented in Ref. [11]. The calculated differential cross sections are persistently smaller than the measured values. This might imply that a tuning of the Argonne v_{14} potential is needed although the analyzing powers are described well with it. Otherwise it might be needed to make modification of the three-body Faddeev calculations because in the calculation only two-body force is considered.

It is generally difficult to modify the NN interactions because of the constraint of their normalization. Therefore, here, considerations are made focusing to the modification of the three-body calculations.

One plausible explanation for this disagreement might be due to the S-wave component of deuteron-proton interaction. One of the candidates to correct the S-wave interaction is the inclusion of the three-nucleon interactions (TNI), for example, the delta degrees of freedom. Note that TNI is not included in the present calculations. The delta intermediate state in the three-body scattering at intermediate energies is much more important than it is at low energies. The delta intermediate state is generated by exchanging two pions among the three nucleons as shown in Fig. 5.3.

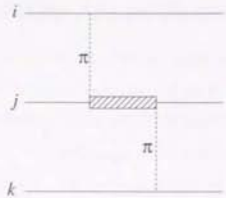

Figure 5.3: Two-pion exchange three-nucleon force. Delta is generated in the intermediate state.

In TNI as an interaction of two-pion exchange, $L = 0$ component is dominant so that TNI is directly related to the S-wave component of the partial wave interactions between deuteron and proton of ${}^2S_{1/2}$. TNI is known to be important to predict the property of the binding energy of the three-nucleon bound state whose spin party is ${}^2S_{1/2}$ [15].

At a low energy region, a discrepancy between the calculation and the data was pointed out in the ${}^2S_{1/2}$ wave [13, 14]. In Ref. [13], a phase shift analysis has bee made for the d-p elastic scattering at $E_p^{\rm lab} = 3$ MeV and consequently a discrepancy between the result of the phase shift analysis and the Faddeev calculation in ${}^2S_{1/2}$ partial wave interaction was found. In Ref. [14], a disagreement between the data and the calculation in the differential cross sections at $E_d^{\rm lab} = 5 \sim 18$ MeV is also reported. It is pointed out that one important reason for the disagreement is the wrong prediction of the S-wave component of the deuteron-proton interactions.

At present, the effect of the delta degrees of freedom on the three-nucleon system has been examined only for the bound state [41]. The inclusion of the delta degrees of freedom should be made for the three-body scattering state in order to see whether the puzzle can be proved by the inclusion of the delta in the calculation for the three-body scattering processes.

It should be noted that another possible explanation is the relativistic effect. Although, at present, the size of the relativistic effect on the differential cross sections and on the analyzing powers can not be estimated. The relativistic treatment has not been established yet and it still remains one of the future interests.

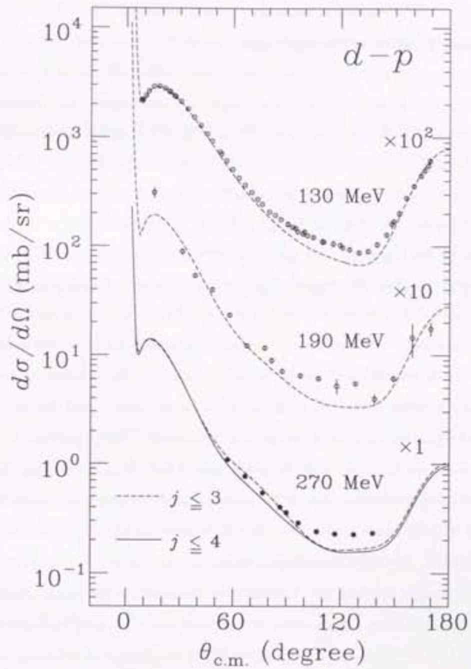

Figure 5.4: Differential cross sections at $E_d^{\rm lab} = 130$ MeV [39], 190 MeV [40], and 270 MeV (present) data with the predictions of the three-body calculation.

Chapter 6

Summary and conclusions

With an interest in how well few-nucleon systems can be described by using two-body NN interactions determined by NN scattering data, the differential cross sections and the vector and tensor analyzing powers A_y, A_{yy}, A_{xx}, and A_{xz} for the d-p elastic scattering were measured at $E_d^{\rm lab} = 270$ MeV. This is the first measurement of a complete set of the deuteron analyzing powers for the d-p elastic scattering at an intermediate energy. All components of the analyzing powers show large absolute values at around $\theta_{\rm c.m.} = 90^\circ$ and vary smoothly with the scattering angle. These features, large and smooth behavior of the analyzing powers, are extremely useful for the accurate determination of the deuteron polarizations. The polarimeter making use of the d-p elastic scattering, therefore, allows us to measure very efficiently the vector and tensor components of the deuteron polarizations simultaneously.

The results are compared with the predictions of the PWIA calculations. In the single scattering description, one of the nucleons in the deuteron undergoes single scattering with the target proton. Note that there exists no adjustable parameters in the calculations. The experimental data, except for A_{yy} and A_{xx}, are roughly reproduced at the angles less than 90°. Consideration was made for the neutron exchange process which have large cross sections at backward angles. In order to improve the fit, it might be needed to include the effects of the interference of the direct elastic and the neutron exchange processes as well as deuteron D-state. The experimental

data at forward angles and backward angles are desirable for further investigation.

The data are also compared with the three-body Faddeev calculation with no adjustable parameters. While the fit of the Faddeev calculations to the data at low energies is poor, a good reproduction of the data is obtained at $E_d^{\rm lab} = 270$ MeV. However, the fit of the differential cross section is not satisfactory. This is surprising since, in general, it is more difficult to obtain a good reproduction of the analyzing powers than the differential cross sections. At present, the explanation of the disagreement is not understood yet. The inclusion of the three-nucleon interaction might improve the fit since its importance has been reported in the low energy region [13, 14, 15]. It is also interesting to investigate whether the fit is improved by an explicit inclusion of the delta degrees of freedom [41]. It should be also noted that it is important to study the role of relativity which is one of the current issues in the study of the few-nucleon systems [42]. We hope that our data with high statistical accuracy stimulate theoreticians to do a calculation by taking these effects into account.

Acknowledgment

I am particularly indebted to Professor Hideyuki Sakai, who proposed this experiment and provided me with an opportunity to study this interesting subject. He also gave me encouragement and excellent advice during the course of the study. I also express my gratitude to Dr. Hiroyuki Okamura, who gave me appropriate advice and physics training.

I would like to express my gratitude to the collaborators of this experiment. I am indebted to all following collaborators. Professor Hideyuki Sakai gave me a chance to take major part of this experiment and encouraged me during the experiment. Dr. Hiroyuki Okamura gave me guidance and help throughout this experiment. Especially the excellent data taking and data analyzing system "Polly-Anna" was written by him. I would like thank Mr. Tomohiro Uesaka for his assistance. I was largely helped by him. I also thank Mr. Satoru Ishida, Mr. Hideaki Otsu, Mr. Tomotugu Wakasa, Mr. Yoshiteru Satou, Mr. Takashi Niizeki, Mr. Kenichi Katoh, Mr. Toshiyuki Yamashita, and Mr. Takamasa Nonaka.

I thank Professor Kichiji Hatanaka for his collaboration and useful advice.

I would like to thank Professor Yasuro Koike who made the three-body calculation and taught about the Faddeev calculation.

I wish to acknowledge Mr. Atsuhi Itabashi for valuable discussions on the impulse approximation calculation.

I wish to appreciate the staff of the RARF. In particular, Dr. Yasushige Yano, who is the director of the facility, gave me continuous encouragement. Mr. Kumio Ikegami and Mr. Jiro Fujita helped me in constructing the polarized ion source.

I would like to express best regards to Professor T. B. Clegg for his advice concerning with the construction and operation of the polarized ion source.

Lastly, but not least, I thank my friends in RIKEN and my family for their continuous encouragement during the course of the study.

References

[1] Recent review was made by H. Sakai, AIP Conf. Proc. **339**(1995) p. 482.

[2] L. Punjabi, R. Abegg, S. Belostotsky, M. Boivin, A. Boundard, E. Cheung, V. Ladygin, J. Oh, L. Penchev, N. Piskunov, C. F. Perdrisat, I. Sitnik, E. A. Strokovsky, E. Tomasi-Gustafsson, V. Vikhrov, J. Yonnet, and A. Zghiche, Phys. Lett. **B350**(1995)178.

[3] Y. Iseri, M. Tanifuji, H. Kameyama, M. Kamimura, M. Yahiro, Nucl. Phys. **A533**(1991)574; M. Tanifuji, H. Kameyama, M. Kamimura, Y. Iseri, and M. Yahiro, Phys. Lett. **B217**(1989)375; M. Tanifuji and Y. Iseri, Prog. Theor. Phys. **87**(1992)247.

[4] M. Morlet, E. Tomasi-Gustafsson, A. Willis, J. Van de Wiele, N. Marty, C. Glashausser, B. N. Jhonson, F. T. Baker, D. Beatty, L. Bimbot, C. Djalali, G. W. R. Edwards, A. Green, J. Guillot, F. Jourdan, H. Langevin-Joliot, L. Rosier, and M. Y. Youn, Phys. Rev. **C46**(1992)1008; M. Morlet, A. Willis, J. Van de Wiele, N. Marty, J. Guillot, H. Langevin-Joliot, L. Bimbot, E. Tomasi-Gustafsson, G. W. R. Edwards, R. W. Fergerson, C. Glashausser, D. Beatty, A. Green, C. Djalali, F. T. Baker, and J. C. Duchazeaubeneix, Phys. Lett. **B247**(1990)228.

[5] H. Okamura, S. Fujita, Y. Hara, K. Hatanaka, T. Ichihara, S. Ishida, K. Katoh, T. Niizeki, H. Ohnuma, H. Otsu, N.S., Y. Satou, T. Uesaka, T. Wakasa, T. Yamashita, and H. Sakai, Phys. Lett. **B345**(1995)1.

[6] G. Igo, A. Masaike, B. Aas, E. Bleszinski, M. Bleszinski, M. Gazzaly, S. J. Greene, H. Hasai, S. Ishimoto, S. Isagawa, K. Jones, D. Lopiano, J. B. McClelland, F. Nishiyama, Y. Ohashi, A. Okihana, G. Pauletta, F. Sperisen, Tsu-Hsun Sun, N. Tanaka, G. S. Weston, and C. A. Whitten, Jr., Phys. Rev. **C38**(1988)2777.

[7] M. Haji-Saied, E. Bleszynski, M. Bleszynski, J. Carroll, G. J. Igo, T. Jaroszewicz, and A. T. M. Wang, Phys. Rev. **C36**(1987)2010.

[8] G. Alberi, M. Bleszinski, and T. Jaroszewicz, Ann. Phys. (N.Y.) **142**(1982)299.

[9] See, for example, J. S. Levinger, Springer Tracts in Modern Physics, vol.71, ed. G. Höhler, (Springer, New York, 1974) p. 88; W. Glöckle, The Quantum Mechanical Few-Body Problem, (Springer, New York, 1983) p. 83.

[10] W. Glöckle, H. Witala, H. Kamada, D. Hüber, and J.Golak AIP Conf. Proc. **334**(1994) p. 45.

[11] H. Witala, W. Glöckle, L. E. Antonuk, J. Arvieux, D. Bachelier, B. Bonin, A. Boudard, J. M. Cameron, H. W. Fielding, M. .Garçn, F. Jourdan, C. Lapointe, W. J. MacDonald, J. Pasos, G. Roy, I. The, J. Tinslay, W. Tornow, J. Yonnet, and W. Zeigler, Few Body Systems **15**(1993)67.

[12] S. N. Bunker, J. M. Cameron, R. F. Carlosn, J. Reginald Richardson, P. Tomš, W. T. H. Van Oers, and J. W. Verba, Nucl. Phys. **A113**(1968)461.

[13] L. D. Knutson, L. O. Lamm, and J. E. McAninch, Phys. Rev. Lett. **71**(1993)3762.

[14] K. Sagara, H. Oguri, S. Shimizu, K. Maeda, H. Nakamura, T. Nakashima, and S. Morinobu, Phys. Rev. **C50**(1994)576.

[15] A. Kievsky and M. Vviani, Phys. Rev. **C52**(1995)R15.

[16] V. Derenchuk, R. Brown, and M. Wedekind, AIP Conf. Proc. **293**(1994) p. 84.

[17] T. B. Clegg, AIP Conf. Proc. **187**(1989) p. 1227.

[18] J. M. Cameron, B. Ni, L. E. Antonuk, E. B. Cairns, H. W. Fielding, L. Holm, R. Igarashi, C. Lapointe, W. J. McDonald, J. Pasos, N. L. Rodning, G. Roy, J. Soukup, and W. Ziegler, J. Arvieux, J. Tinslay, J. Yonnet, B. Bonin, A. Boudard, M. Garçn, D. Bachelier, and I. The, Nucl. Instr. and Meth. **A305**(1991)257.

[19] N.S., H. Okamura, H. Sakai, T. Uesaka, T. Kubo, N. Inabe, K. Ikegami, J. Fujita, M. Kase, A. Goto, Y. Yano, and K. Hatanaka, RIKEN Accel. Prog. Rep. **26**(1992)138.

[20] J. Bystricky, F.Lehar, A. de Lesquen, A. Penzo, L. van Rossum, J. M. Fontine, F. Perot, G. Leleux, and A. Nakach, Nucl. Instr. and Meth. **A234**(1985)412.

[21] V. G. Ableev, S. Dzhemukhadze, V. P. Ershov, V. V. Fimushkin, B. Kühn, M. V. Kulikov, A. A. Nomofilov, L. Penchev, Yu. K. Pilipenko, N. M. Piskunov, V. I. Sharov, V. B. Shutov, I. M. Sitnik, E. A. Strokovsky, L. N. Strunov, and S. A. Zaporozhets, Nucl. Instr. and Meth. **A306**(1991)73.

[22] H. Okamura *et al.*, contribution paper to the 7th Int. Conf. on polarization phenomena in nuclear physics (Paris 1990).

[23] Proc. of the third Int. Conf. on polarization phenomena in nuclear reactions, eds. H. H. Varschall and W. Haeberli (Univ. Winsconsin Press, Madison 1971).

[24] G. G. Ohlsen, Rep. Prog. Phys. **35**(1972)717; G. G. Ohlsen and P. W. Keaton, Jr., Nucl. Instr. and Meth. **109**(1973)41.

[25] H. Okamura, H. Sakai, N.S., T. Uesaka, S. Ishida, H. Otsu, T. Wakasa, K. Hatanaka, T. Kubo, N. Inabe, K. Ikegami, J. Fujita, M. Kase, A. Goto, and Y. Yano, AIP Conf. Proc. **293**(1994) p. 84.

[26] H. Okamura, N.S., T. Uesaka, H. Sakai, K. Hatanaka, A. Goto, M. Kase, N. Inabe, and Y. Yano, AIP Conf. Proc. **343**(1995) p. 123.

[27] S. Ishida, S. Fujita, Y. Hara, K. Hatanaka, T. Ichihara, K. Katoh, T. Niizeki, H. Okamura, H. Otsu, H. Sakai, N.S., Y. Satou, T. Uesaka, T. Wakasa, and T. Yamashita, AIP Conf. Proc. **343**(1995) p. 182.

[28] D. V. Bugg and C. Wilkin, Nucl. Phys. **A467**(1987)575.

[29] J. Carbonell, M. B. Barbaro, and C. Wilkin Nucl. Phys. **A529**(1991)653.

[30] A. K. Kerman, H. McManus, and R. M. Thaler, Ann. Phys. (N.Y.) **8**(1959)551.

[31] see, for example, R. Hagedorn, Relativistic Kinematics, (W. A. Benjamin INC., Massachusetts, 1963) p. 65.

[32] S. A. Gurvitz Phys. Rev. **C33**(1986)422.

[33] R. A. Arndt and L. D. Roper, *Scattering Analysis Interactive Dial-In program* (SAID), Virginia Polytechnic Institute and State University (unpublished).

[34] Y. Koike, D. R. Lehman, L. C. Maximon, and W. C. Parke AIP Conference Proceedings **334**(1994) p. 836.

[35] W. Grübler, Nucl. Phys. **A353**(1981)31c.

[36] R. B. Wiringa, R. A. Smith, and T. A. Ainsworth, Phys. Rev. **C29**(1984)1207.

[37] Y. Koike, W. C. Parke, L. C. Maximon and D. R. Lehman, in preparation.

[38] Y. Koike, Prog. Theor. Phys. **87**(1992)775.

[39] H. Shimizu, K. Imai, N. Tamura, K. Nishimura, K. Hatanaka, T. Saito, Y. Koike, and Y. Taniguchi Nucl. Phys. **A382**(1982)242.

[40] O. Chamberlain and M. O. Stern, Phys. Rev. **94**(1954)666.

[41] C. H. Hajduk and P. U. Sauer, Nucl. Phys. **A322**(1979)329; A. Stadler and P. U. Sauer, Phys. Rev. **C46**(1992)64; A. Picklesimer, R. A. Rice, and R. Brandenburg, Few Body Systems **19**(1995)47.

[42] J. A. Tjon, AIP Conf. Proc. **334**(1994) p. 177.

[43] M. Lacombe, B. Loiseau, J. M. Richard, R. Vinh Mau, J. Côté, P. Pirés, and R. de Tourreil, Phys. Rev. **C21**(1980)861.

[44] M. Lacombe, B. Loiseau, R. Vinhmau, J. Côté, P. Pirés, and R. de Tourreil, Phys. Lett. **101B**(1981)139.

[45] N. S., Master thesis of University of Tokyo, unpublished (in Japanese).

[46] M. Simonius, Polarization Nuclear Physics, in Lecture Notes in Physics 30, ed. D. Fick (Springer, 1974), p. 38.

[47] K. Stephenson, L. D. Knutson, and W. Haebrli, Nucl. Phys. **A227**(1977)365.

[48] M. Fujiwara, H. Akimune, Y. Fujita, K. Hatanaka, T. Noro, H. Ikegami, N. Matsuoka, S. Hirata, A. Tamii, H. Sakaguchi, Y. Sakemi, A. Yamagoshi, S. Yamamura, and M. Yosoi, RCNP annual report (1992) p. 170.

[49] K. Hatanaka, K. Takahisa, H. Tamura, H. Kaneko, and I. Miura AIP Conf. Proc. **339**(1995) p. 702.

Appendices

A. Spin polarization for $S = 1$ – The Madison convention –

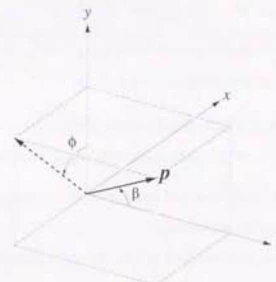

Figure 6.1: Definition of the spin angles β and ϕ. The deuteron is scattered in the x-z plane.

Following the Madison convention, the form of the differential cross sections is written as

$$\begin{aligned}\frac{d\sigma_{\mathrm{pol}}(\theta)}{d\Omega} = \frac{d\sigma_{\mathrm{unpol}}(\theta)}{d\Omega}[1 &+ \frac{3}{2}p_y\, A_y(\theta) + \frac{2}{3}p_{xz}\, A_{xz}(\theta) \\ &+ \frac{1}{3}(p_{xx}\, A_{xx}(\theta) + p_{yy}\, A_{yy}(\theta) + p_{zz} A_{zz}(\theta))] \;, \qquad (6.1)\end{aligned}$$

and the vector and tensor polarizations are defined as

$$\vec{p} = \begin{pmatrix} p_x \\ p_y \\ p_z \end{pmatrix} = p_Z \begin{pmatrix} \sin\beta\sin\phi \\ \sin\beta\cos\phi \\ \cos\phi \end{pmatrix}, \qquad (6.2)$$

$$
\begin{aligned}
p_{xy} &= -\frac{3}{2}\, p_{ZZ} \sin^2\beta \cos\phi \sin\phi, \\
p_{yz} &= \frac{3}{2}\, p_{ZZ} \sin\beta \cos\beta \cos\phi, \\
p_{xz} &= -\frac{3}{2}\, p_{ZZ} \sin\beta \cos\beta \sin\phi, \\
p_{xx} &= \frac{1}{2}\, p_{ZZ} \left(3\sin^2\beta \sin^2\phi - 1\right), \\
p_{yy} &= \frac{1}{2}\, p_{ZZ} \left(3\sin^2\beta \cos^2\phi - 1\right), \\
p_{zz} &= \frac{1}{2}\, p_{ZZ} \left(3\cos^2\beta - 1\right) \quad ,
\end{aligned}
\tag{6.3}
$$

where β and ϕ are the spin angle shown in Fig. 6.1, p_Z and p_{ZZ} are vector and tensor polarizations, respectively, defined as

$$
\begin{aligned}
&p_Z = N_+ - N_- \,, \quad p_{ZZ} = 1 - 3N_0 \,, \\
&\text{where} \quad N_+ + N_0 + N_- = 1 \,.
\end{aligned}
\tag{6.4}
$$

N_+, N_-, and N_0 are the occupation probabilities of the deuteron substates with the spin projections 1, -1, and 0, respectively.

The quantities defined are normalized so that the vector quantities (p_x, p_y, p_z, and A_y) may vary between +1 and -1, the tensor quantities (p_{xy}, p_{xz}, p_{yz}, and A_{xz}) may vary between $+\frac{3}{2}$ and $-\frac{3}{2}$, and the tensor quantities (p_{xx}, p_{yy}, p_{zz}, A_{xx}, A_{yy}, and A_{zz}) may vary between +1 and -2. The spherical and Cartesian tensor analyzing powers are related as follows:

Cartesian to spherical

$$
\begin{aligned}
T_{10} &= 0 \\
T_{1\pm1} &= -i\frac{\sqrt{3}}{2} A_y \\
T_{20} &= \frac{1}{\sqrt{2}} A_{zz} \\
T_{2\pm1} &= \mp\frac{1}{\sqrt{3}} A_{xz} \\
T_{2\pm2} &= \mp\frac{1}{2\sqrt{3}} (A_{xx} - A_{yy})
\end{aligned}
\tag{6.5}
$$

spherical to Cartesian

$$
\begin{aligned}
A_y &= \frac{2}{\sqrt{3}}\, i\, T_{11} \\
A_{yy} &= -\sqrt{3}\, T_{22} - \frac{1}{\sqrt{2}}\, T_{20} \\
A_{xx} &= \sqrt{3}\, T_{22} - \frac{1}{\sqrt{2}}\, T_{20} \\
A_{zz} &= \sqrt{2}\, T_{20} \\
A_{xz} &= -\sqrt{3}\, \mathrm{Re}\,(T_{21})
\end{aligned}
\tag{6.6}
$$

The tensor analyzing power A_{xx}, A_{yy}, and A_{zz} satisfy the identity

$$
A_{xx} + A_{yy} + A_{zz} = 0 \,. \tag{6.7}
$$

Thus four of the analyzing powers which appears above for the polarized deuteron scattering with unpolarized target are independent.

B. Magnetic elements of RIKEN PIS

(Sextupole magnets)

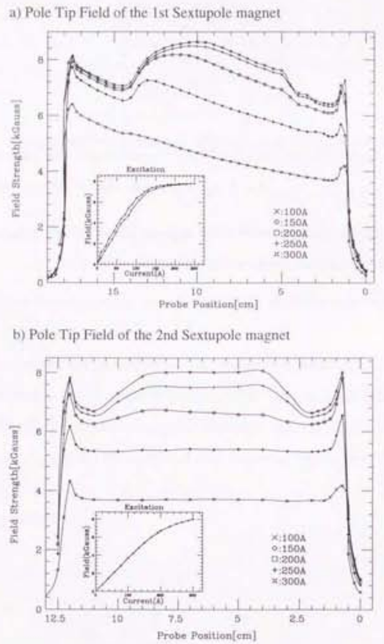

Figure 6.2: The pole tip fields of the first (a) and the second (b) sextupole magnets. The entrance aperture of the first magnet is small as 14 mmϕ so as to have a strong field.

(Adiabatic passage field for the strong field transition)

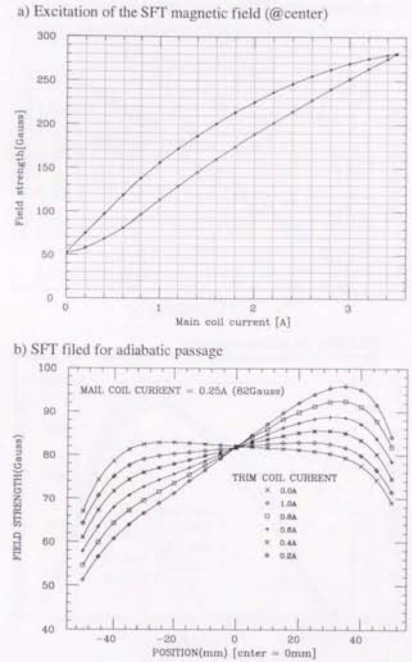

Figure 6.3: (a) Excitation function of the SFT magnetic field measured at the center of the magnetic pole. (b) The magnetic field strength of the adiabatic passage SFT. The field gradient can be varied independent form the center field strength.

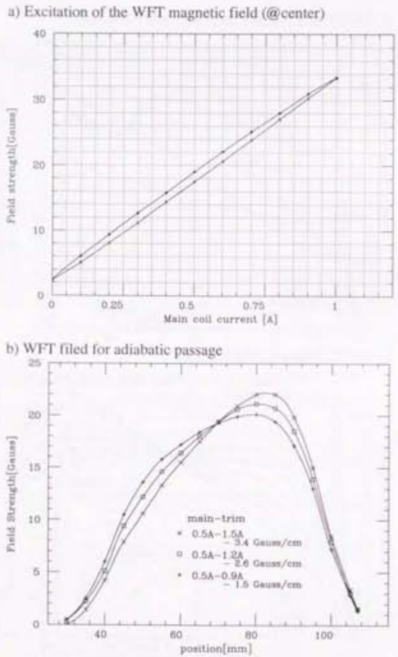

Figure 6.4: (a) Excitation function of the WFT magnetic field measured at the center of the magnetic pole. (b) The magnetic field strength of the adiabatic passage WFT. The field gradient can be varied independent form the center field strength.

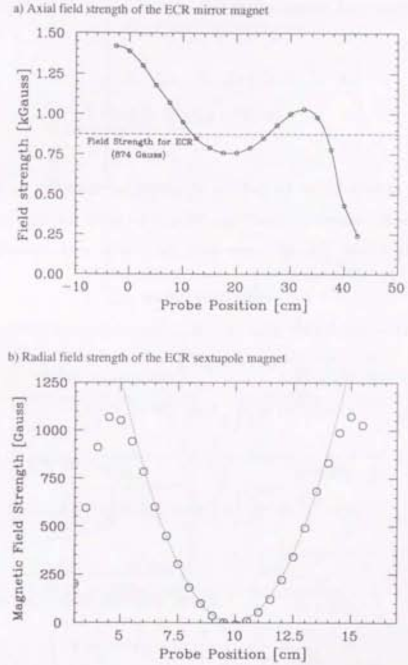

Figure 6.5: (a) Axial magnetic field strength of the ECR mirror magnet with a typical parameters of 111 A (1st coil) and 96 A (2nd coil). (b) Radial magnetic field strength of the ECR sextupole permanent magnet ($B_R = 53.11$ Gauss/cm^2).

C. Hyper fine structure of the deuterium atom

The spin dependent part of the Hamiltonian of atomic deuterium with a magnetic field $\vec{B}$ in terms of total, nuclear and electron spin operators $\vec{F}$, $\vec{I}$, and $\vec{J}$ is represented as

$$\begin{aligned} H &= -(\vec{\mu}_I + \vec{\mu}_J)\cdot\vec{B} - \alpha'\vec{\mu}_I\cdot\vec{\mu}_J \\ &= -\left(g_I\mu_N\vec{I} + g_J\mu_B\vec{I}\right)\cdot\vec{B} + \alpha\vec{I}\cdot\vec{J} \ , \end{aligned} \tag{6.8}$$

where g_I are g_J are g-factors for deuteron and electron, respectively, μ_N and μ_B are nuclear and Bohr magneton, respectively, and α is the hyper fine splitting energy of $\Delta W = h\times$ 327.4 MHz. The eigen-states of the Hamiltonian are analytically obtained as

$$\begin{aligned}
|1> &= |1,1>_I|\tfrac{1}{2},\tfrac{1}{2}> \\
|2> &= \frac{1}{\sqrt{a_2^2+b_2^2}}(a_2|1,1>_I|\tfrac{1}{2},-\tfrac{1}{2}>_J + b_2|1,0>_I|\tfrac{1}{2},\tfrac{1}{2}>_J) \\
& \qquad a_2 = \frac{\sqrt{2}}{3}, b_2 = \frac{1}{2}\left(\frac{1}{3}+x+\sqrt{x^2+\frac{2}{3}x+1}\right) \\
|3> &= \frac{1}{\sqrt{c_3^2+d_3^2}}(c_3|1,0>_I|\tfrac{1}{2},-\tfrac{1}{2}>_J + d_3|1,-1>_I|\tfrac{1}{2},\tfrac{1}{2}>_J) \\
& \qquad c_3 = \frac{\sqrt{2}}{3}, d_3 = \frac{1}{2}\left(-\frac{1}{3}+x+\sqrt{x^2-\frac{2}{3}x+1}\right) \\
|4> &= |1,-1>_I|\tfrac{1}{2},-\tfrac{1}{2}> \\
|5> &= \frac{1}{\sqrt{c_5^2+d_5^2}}(c_5|1,0>_I|\tfrac{1}{2},-\tfrac{1}{2}>_J + d_5|1,-1>_I|\tfrac{1}{2},\tfrac{1}{2}>_J) \\
& \qquad c_5 = \frac{\sqrt{2}}{3}, d_5 = -\frac{1}{2}\left(-\frac{1}{3}+x-\sqrt{x^2-\frac{2}{3}x+1}\right) \\
|6> &= \frac{1}{\sqrt{a_6^2+b_6^2}}(a_6|1,1>_I|\tfrac{1}{2},-\tfrac{1}{2}>_J + b_6|1,0>_I|\tfrac{1}{2},\tfrac{1}{2}>_J) \\
& \qquad a_6 = \frac{\sqrt{2}}{3}, b_6 = -\frac{1}{2}\left(\frac{1}{3}+x-\sqrt{x^2+\frac{2}{3}x+1}\right) \ .
\end{aligned}$$

Here x is the strength of the magnetic field in the unit of B_c = 117 G. The energies and the deuteron polarizations for the six eigen states are shown in Fig. 6.6 as a function of the magnetic field strength of $x = B/B_c$.

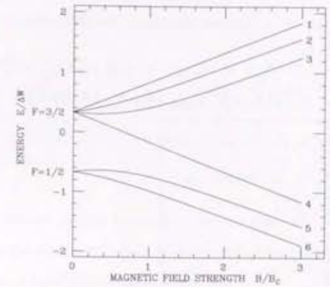

Figure 6.6: Hyper fine states. $\Delta W = h\times$327.4 MHz and B_c = 117 G

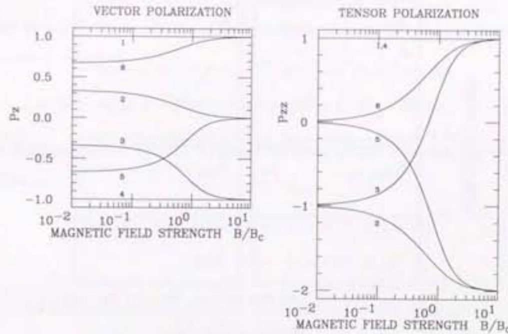

Figure 6.7: Vector and tensor polarization of the deuteron

D. $^{12}C(d,p)^{13}C_{gnd}$ at E_d^{lab}= 14 MeV

The absolute values of the deuteron polarization have been obtained on the basis of the analyzing powers of the $^{12}C(d,p)^{13}C_{gnd}$ reaction which were measured at the Kyushu University tandem accelerator laboratory. Detail description on the experiment can be found in [45].

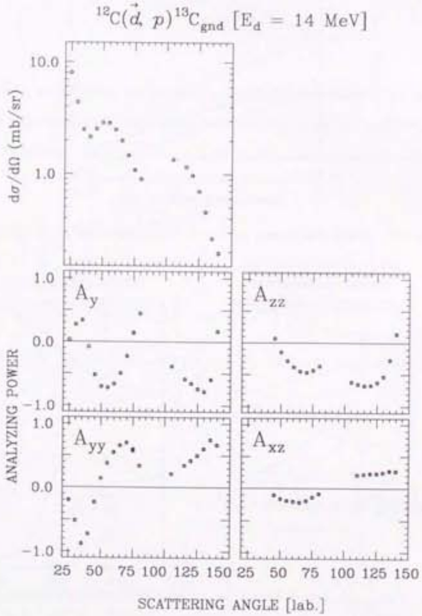

Figure 6.8: Differential cross sections and the analyzing powers for the $^{12}C(d,p)^{13}C_{gnd}$ reaction.

E. NN scattering amplitudes

The NN scattering amplitudes of Bystricky parameters A_B, B_B, C_B, D_B, E_B are obtained by using a code SAID [33]. In the convention of Bystricky, NN amplitude is written as;

$$\begin{aligned} f_{j3}^{NN} = \frac{1}{2}((A_B + B_B) &+ E_B\left(\vec{\sigma}^{j}\cdot\hat{n} + \vec{\sigma}^{3}\cdot\hat{n}\right) \\ &+ (A_B - B_B)(\vec{\sigma}^{j}\cdot\hat{n})(\vec{\sigma}^{3}\cdot\hat{n}) \\ &+ (C_B + D_B)(\vec{\sigma}^{j}\cdot\hat{q})(\vec{\sigma}^{3}\cdot\hat{q}) \\ &+ (C_B - D_B)(\vec{\sigma}^{j}\cdot\hat{p})(\vec{\sigma}^{3}\cdot\hat{p})). \end{aligned} \tag{6.9}$$

Here the amplitudes are complex functions of two variables, e.g. the scattering angle θ_{NN} in the NN center of mass system and the scattering energy T_{NN} in the target-rest frame. The center of mass system basis vectors are:

$$\hat{n} = \frac{\vec{k}_i \times \vec{k}_f}{\vec{k}_i \times \vec{k}_f}, \quad \hat{q} = \frac{\vec{k}_f - \vec{k}_i}{\vec{k}_f - \vec{k}_i}, \quad \hat{p} = \hat{q} \times \hat{n} \ , \tag{6.10}$$

where $\vec{k}_i$ and $\vec{k}_f$ are the initial and final momenta, respectively. The amplitudes are normalized such that

$$d\sigma/d\Omega_{NN} = |A_B|^2 + |B_B|^2 + |C_B|^2 + |D_B|^2 + |E_B|^2 \quad (\mathrm{fm}^2/\mathrm{sr}) \tag{6.11}$$

The KMT parameters A, B, C, E, and F, by which the NN scattering amplitude is written as;

$$\begin{aligned} f_{j3}^{NN}(T,\theta) = A + C(\vec{\sigma}^{j}\cdot\hat{n} + \vec{\sigma}^{3}\cdot\hat{n}) + B(\vec{\sigma}^{j}\cdot\hat{n})(\vec{\sigma}^{3}\cdot\hat{n}) \\ + E(\vec{\sigma}^{j}\cdot\hat{q})(\vec{\sigma}^{3}\cdot\hat{q}) + F(\vec{\sigma}^{j}\cdot\hat{p})(\vec{\sigma}^{3}\cdot\hat{p}). \end{aligned} \tag{6.12}$$

The KMT parameters and the Bystricky parameters are related thorough

$$\begin{aligned} A &= \frac{1}{2}(A_B + B_B) \\ B &= \frac{1}{2}(A_B - B_B) \end{aligned}$$

$$
\begin{aligned}
C &= \frac{1}{2}E_B \\
E &= \frac{1}{2}(C_B + D_B) \\
F &= \frac{1}{2}(C_B - D_B) \ .
\end{aligned}
\tag{6.13}
$$

The differential cross sections are

$$
d\sigma/d\Omega_{NN} = \frac{1}{2}\left(|A|^2 + |B|^2 + 2|C|^2 + |D|^2 + |E|^2\right) \quad (\mathrm{fm}^2/\mathrm{sr}) \tag{6.14}
$$

By using the KMT parameters The impulse approximation calculations in chapter 4 for the d-p elastic scattering were made by using the KMT parameters.

F. Parameterized deuteron wave function

The deuteron wave function can be represented by summation of S-state ($L = 0$) and D-state ($L = 2$) components as:

$$
\psi = \psi_S + \psi_D \tag{6.15}
$$

and each components is given as follows:

$$
\psi_S = \frac{U(r)}{r} Y_0^0 \chi_1^1 = \sqrt{\frac{1}{4\pi}} \frac{U(r)}{r} \chi_1^1 \tag{6.16}
$$

$$
\psi_D = \frac{W(r)}{r} \left(\sqrt{\frac{6}{10}} Y_2^2 \chi_1^{-1} - \sqrt{\frac{3}{10}} Y_2^1 \chi_1^0 + \sqrt{\frac{1}{10}} Y_2^0 \chi_1^1 \right) \tag{6.17}
$$

$$
\begin{cases}
Y_2^2 = \sqrt{\frac{15\pi}{32}} \sin^2\theta e^{2i\phi} \\
Y_2^1 = \sqrt{\frac{15\pi}{8}} \cos\theta \sin\theta e^{2i\phi} \\
Y_2^0 = \sqrt{\frac{5\pi}{16}} (3\cos^2\theta - 1)
\end{cases} .
$$

The radial parts of the deuteron wave function are parameterized based on Paris NN potential [43] in Ref. [44]. The radial parts of the deuteron wave function, $U(r)$ and $W(r)$ is given in both configuration space and momentum spaces as follows.

$$
\begin{aligned}
U(r) &= \sum_{j=1}^{13} C_j \exp(-m_j r) \\
W(r) &= \sum_{j=1}^{13} D_j \exp(-m_j r) \left(1 + \frac{3}{m_j r} + \frac{3}{m_j^2 r^2}\right)
\end{aligned}
\tag{6.18}
$$

$$
\begin{aligned}
\hat{U}(r) &= \sqrt{\frac{2}{\pi}} \sum_{j=1}^{13} \frac{C_j}{p^2 + m_j^2} \\
\hat{W}(r) &= \sqrt{\frac{2}{\pi}} \sum_{j=1}^{13} \frac{D_j}{p^2 + m_j^2}
\end{aligned}
\tag{6.19}
$$

The masses m_j are chosen as $m_j = \alpha + (j-1)m_o$, with $m_o = 1 fm^{-1}$, where α is a typical deuteron diameter defined by

$$
\alpha = \sqrt{2m_R|E_D|}/\hbar = 0.23162461 fm^{-1}. \tag{6.20}
$$

m_R : reduced mass

E_D : the deuteron binding energy

The values of the parameters C_j and D_j are listed in Table 6.1.

Table 6.1: Coefficients of the parameterized deuteron wave function.

j	C_j	D_j
1	0.88688076e+00	0.23135193e−01
2	−0.34717093e+00	−0.85604572e+00
3	−0.30502380e+01	0.56068193e+01
4	0.56207766e+02	−0.69462922e+02
5	−0.74957334e+03	0.41631118e+03
6	0.53365279e+04	−0.12546621e+04
7	−0.22706863e+05	0.12387830e+04
8	0.60434469e+05	0.33739172e+04
9	−0.10292058e+06	−0.13041151e+05
10	0.11223357e+06	0.19512524e+05
11	−0.75925226e+05	−1.56343237e+04
12	0.29059715e+05	6.62310892e+03
13	−4.81573680e+03	−1.16981847e+03

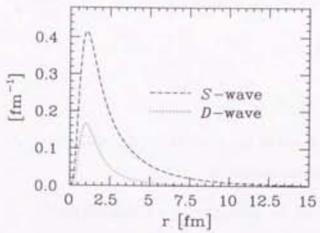

Figure 6.9: Radial part of the deuteron wave function in configuration space.

G. Spin projection operator T^{12}

The triplet spin projection operator T^{12} defined as

$$T^{12} = \frac{1}{4}(3 + \vec{\sigma}_1 \cdot \vec{\sigma}_2) \tag{6.21}$$

has eigenvalues of 1 and 0 for the triplet and singlet deuteron spin functions:

$$\begin{aligned} T^{12}\,|S_d = 1,\, M_d = +1\rangle &= |M_d = +1\rangle \\ T^{12}\,|S_d = 1,\, M_d = \;\;0\rangle &= |M_d = \;0\rangle \\ T^{12}\,|S_d = 1,\, M_d = -1\rangle &= |M_d = -1\rangle \\ T^{12}\,|S_d = 0,\, M_d = 0\rangle &= 0 \;. \end{aligned} \tag{6.22}$$

Therefore $T^{12}\,|1/2, m_1\rangle|1/2, m_2\rangle$ becomes;

$$\begin{aligned} T^{12}|1/2,+1/2\rangle|1/2,+1/2\rangle &= |1/2,+1/2\rangle|1/2,+1/2\rangle \\ T^{12}|1/2,\pm1/2\rangle|1/2,\mp1/2\rangle &= \frac{1}{2}\left(|1/2,+1/2\rangle|1/2,-1/2\rangle + |1/2,-1/2\rangle|1/2,+1/2\rangle\right) \\ T^{12}|1/2,-1/2\rangle|1/2,-1/2\rangle &= |1/2,-1/2\rangle|1/2,-1/2\rangle \;. \end{aligned} \tag{6.23}$$

It is also easily obtained that

$$(T^{12})^n = T^{12} \;. \tag{6.24}$$

H. Analyzing power measurement at $E_d = 200$ MeV

The analyzing power $A_y(90^\circ)$ and $A_{yy}(90^\circ)$ for the d-p elastic scattering has been determined at $E_d^{\rm lab} = 200$ MeV. The final goal of this measurement is a direct calibration of the absolute values of the vector and tensor polarization of the deuteron beams.

It is known that the analyzing powers for the deuteron induced reactions with the spin parity structure

$$1^+ + 0^+ \rightarrow 0^+ + 0^- , \tag{6.25}$$

for example the $^{16}O(d,\alpha_3)^{14}N^*$ reaction, have the following model-independent relations[46].

$$T_{20} + \sqrt{6}\,T_{22} = -\sqrt{2} \quad (\Leftrightarrow A_{yy} = -1) \tag{6.26}$$

$$|iT_{11}|^2 + \frac{1}{2}|T_{20}|^2 + |T_{21}|^2 + |T_{22}|^2 = 1 \tag{6.27}$$

The tensor polarization can be calibrated by utilizing the first relation and, consequently, the vector polarization is also calibrated with the help of the second relation.

In a low energy region there are experiments for the purpose of the deuteron polarization calibration by utilizing the $^{16}O(d,\alpha_3)^{14}N^*$ reaction [47]. However in the intermediate energy region such kind of the experiment has not been reported so far. The measurement of the $^{16}O(d,\alpha_3)^{14}N^*$ reaction requires an ultra-high energy resolution since the energy separation of $^{14}N^*$ is small. The energy resolution ±100 keV

Table 6.2: Excited states in $^{14}N^*$.

	Ex (MeV)	j^π
α_0	0.000	1^+
α_1	2.319	0^+
α_2	3.948	1^+
α_3	4.915	0^-
α_4	5.106	2^-

is required to distinguish α_3 from α_4.

In RCNP (Research Center for Nuclear Physics, Osaka university) there is a high resolution spectrograph GRAND RAIDEN [48] which was designed to have momentum resolution $\Delta p/p = 2.5\times10^{-5}$. RCNP Ring cyclotron can accelerate deuteron up to 200 MeV. Highly polarized deuteron beam is provided by a newly constructed polarized ion source [49].

First of all, we obtained a relation between the analyzing powers A_y and A_{yy} at $E_d^{\rm lab} = 270$ MeV and those at $E_d^{\rm lab}= 200$ MeV for the d-p elastic scattering. In the measurement the beam polarization was monitored by using a scattering chamber (a). After bombarding the target at the position (a), the energy of the beam was reduced to 200 MeV by an aluminum degrader at the entrance of the bending magnet (b). The analyzing power at $\theta_{c.m.} = 90^\circ$ were measured by using a scattering chamber which was used as the beam polarization monitor. $Ay(90^\circ)$ and $A_{yy}(90^\circ)$ at $E_d^{\rm lab} =$ 200 MeV were obtained as follows.

Table 6.3: The analyzing powers A_y and A_{yy} at $\theta_{c.m.} = 90^\circ$.

$E_d^{\rm lab}$(MeV)	$A_y(90^\circ)$	$A_{yy}(90^\circ)$
270	-0.391 ± 0.007	0.478 ± 0.016
200	-0.447 ± 0.007	0.427 ± 0.013

Supplement (published paper)

The experimental data of all components of the analyzing powers and the differential cross sections have been published in the paper Physics Letters **B367**(1996)60 with the title "MEASUREMENT OF THE VECTOR AND TENSOR ANALYZING POWERS FOR THE d-p ELASTIC SCATTERING AT $E_d^{\rm lab}$ = 270 MeV" (Editor : R. H. Siemssen, Accepted : 07-Nov-1995).

MEASUREMENT OF THE VECTOR AND TENSOR ANALYZING POWERS FOR THE d-p ELASTIC SCATTERING AT $E_d = 270$ MeV

N. Sakamoto[a], H. Okamura[a], T. Uesaka[a], S. Ishida[a*], H. Otsu[a], T. Wakasa[a], Y. Satou[a], T. Niizeki[b], K. Katoh[b], T. Yamashita[b], K. Hatanaka[c], Y. Koike[d], and H. Sakai[a]

[a]*Department of Physics, University of Tokyo, Bunkyo-ku, Tokyo 113, Japan*

[b]*Department of Physics, Tokyo Institute of Technology, Meguro-ku, Tokyo 152, Japan*

[c]*Research Center for Nuclear Physics, Osaka University, Ibaraki, Osaka 567, Japan*

[d]*Department of Physics, Hosei University, Chiyoda-ku, Tokyo 102, Japan*

Abstract

The differential cross sections and the vector and tensor analyzing powers A_y, A_{yy}, A_{xx}, and A_{xz} for the d-p elastic scattering were measured at $E_d^{\rm lab}$ = 270 MeV over the c.m. angular range from 57° to 138°. The data are compared with a Faddeev calculation. A good description is obtained for all components of the analyzing powers, while a discrepancy of about 30% is found in the cross section around $\theta_{\rm c.m.} = 120°$.

Typeset using REVTEX

*Present address: Cyclotron Laboratory, Institute of Physical and Chemical Research (RIKEN), Wako, Saitama 351-01, Japan

There is a wide interest in how well few-nucleon systems can be described by using nucleon-nucleon (NN) interactions determined by NN scattering data. Among the few-nucleon systems, the nucleon-deuteron (Nd) scattering is a rich source of information on the NN interaction. The vector and tensor spin observables of the Nd scattering are useful to examine the spin dependent part of the NN interaction, the spin-orbit force and the tensor force. In the low energy region the Nd scattering, except for the analyzing power A_y, is well described by a Faddeev calculation with realistic NN interactions [1]. In the intermediate energy region, at an incident deuteron energy (E_d^{lab}) of several hundred MeV, experimental data of deuteron polarization observables for the Nd scattering are scarce. Since the higher partial waves and the large momentum behaviors of the NN interaction become significant with increasing the scattering energy, it is interesting to investigate whether or not observables of the Nd scattering in the intermediate energy region can be described by a Faddeev calculation in a similar manner. Such a study is useful and also helpful for the analysis of the forthcoming CEBAF data on few-nucleon systems since the large momentum behavior is one of the central topics there [2,3].

In this work, differential cross sections and all components of the analyzing powers A_y, A_{yy}, A_{xx}, and A_{xz} for the d-p elastic scattering were measured at $E_d^{lab} = 270$ MeV over the c.m. angular range from 57° to 138° with a high statistical precision and the results were compared with a Faddeev calculation with the Argonne v_{14} potential [4]. The Faddeev calculation with the full NN partial wave interactions of $j \leq 4$ was made by extending a calculation of $j \leq 3$ [5] with a new method of separable expansion USE (unified separable expansion) [6].

The measurement was performed at the RIKEN Accelerator Research Facility (RARF). The vector and tensor polarized deuteron beams were provided by the newly constructed polarized ion source [7,8] and at first accelerated up to 14 MeV by the injector AVF cyclotron and then up to 270 MeV by the main Ring cyclotron. The deuteron beams of intensity of 10–30 nA bombarded a polyethylene (CH_2) target with a thickness of 8.1 mg/cm^2. Four pairs of detectors were placed symmetrically in the directions of azimuthal angles left, right,

up, and down. Each detector consisted of an NE102A plastic scintillator with a thickness of 1 cm coupled to an H1161 photo-multiplier tube. An aluminum block was placed in front of the plastic scintillator to degrade the kinetic energy of the scattered particles such that their energy loss in the plastic scintillator was maximized. The detection of the scattered deuterons and recoil protons in a kinematic coincidence was essential to discriminate the d-p elastic scattering from other scattering processes such as the elastic scattering from carbon or the deuteron break-up process. Scattering angles in the center of mass system $\theta_{c.m.}$ were determined by the angles of recoil protons θ_p. The opening angle of the proton detector $\Delta\theta_p$ was ±1.14°. The deuteron detector was designed to be large enough to cover the solid angle determined by the proton detector. For the special case in which the outgoing deuteron and proton have the same laboratory angle of nearly 30°, the d-p elastic scattering was measured by two pairs of detectors in the horizontal and vertical planes. The two particles could be clearly distinguished by their different energy losses in the plastic scintillator and the differences between their time of flight from the target.

The data were taken with polarized and unpolarized beams of the theoretical maximum values $(p_Z, p_{ZZ}) = (1/3, 1), (0, -2), (-2/3, 0)$, and $(0, 0)$, where p_Z and p_{ZZ} are vector and tensor polarizations, respectively, and are defined as

$$\begin{aligned} p_Z = N_+ - N_-\,, \quad p_{ZZ} = 1 - 3N_0\,, \\ \text{where} \quad N_+ + N_0 + N_- = 1\,. \end{aligned} \tag{1}$$

N_+, N_-, and N_0 are the occupation probabilities of the deuteron substates with the spin projections 1, −1, and 0, respectively. The polarization modes were changed cyclically at intervals of 20 seconds by switching the RF transition units of the ion source. A polarization monitor system, which was installed downstream of the target, also utilized the d-p elastic scattering at $\theta_{c.m.} = \pm 90°$ as a polarization analyzer. The beam polarizations were monitored continuously and were found to be 60–70% of the theoretical maximum values throughout the experiment. The absolute values of the beam polarizations have been calibrated by using the $^{12}C(d,p)^{13}C_{gnd}$ reaction at $E_d^{lab} = 14$ MeV. The energy of 14 MeV corresponds to the injection energy of the main Ring cyclotron. The analyzing powers for the $^{12}C(d,p)^{13}C_{gnd}$ reaction at $E_d^{lab} = 14$ MeV have been measured in advance by using the well calibrated polarized deuteron beam at the Tandem van de Graaf accelerator of Kyushu University [7]. For the polarization monitor system, the analyzing powers A_y and A_{yy} of the d-p elastic scattering at 270 MeV have been determined under the assumption that the deuteron polarization was maintained and stable during the acceleration. The depolarization during the acceleration process is expected to be negligible since the anomalous magnetic moment of the deuteron is small and consequently no depolarization resonance is passed through during the acceleration up to 270 MeV.

The analyzing powers A_y, A_{yy}, and A_{xx} were measured simultaneously with the deuteron spin normal to the horizontal plane. The analyzing powers are defined in the xyz frame of $\hat{\boldsymbol{z}} \,//\, \boldsymbol{k}_i$, $\hat{\boldsymbol{y}} \,//\, \boldsymbol{k}_i \times \boldsymbol{k}_f$, and $\hat{\boldsymbol{x}} \,//\, \hat{\boldsymbol{y}} \times \hat{\boldsymbol{z}}$, where $\boldsymbol{k}_i$ and $\boldsymbol{k}_f$ are the incident and scattered deuteron momenta, respectively. Following the Madison convention [9,10], yields of the d-p elastic scattering with the deuteron polarization (p_Z, p_{ZZ}) can be written as

$$N_{\rm pol}(\theta,\phi) = n_{\rm pol}\,\frac{N_{\rm unpol}(\theta,\phi)}{n_{\rm unpol}}[1 + \frac{3}{2}\,p_Z A_y(\theta)\cos\phi + \frac{1}{2}\,p_{ZZ}(A_{xx}(\theta)\sin^2\phi + A_{yy}(\theta)\cos^2\phi)]\,. \tag{2}$$

Here $N_{\rm pol}$ and $N_{\rm unpol}$ are the yields with polarized and unpolarized beams, respectively, n is the number of deuterons incident on the target, θ is the scattering angle, and ϕ is the azimuthal angle (with respect to the beam) between the normal to the scattering plane and the spin symmetry axis. The azimuthal angles ϕ for four pairs of detectors in the directions of left, right, up, and down are 0, π, $-\pi/2$, and $\pi/2$ radian, respectively. From Eq. (2), by using normalized yields $N'(\theta,\phi) = \frac{N_{\rm pol}(\theta,\phi)/n_{\rm pol}}{N_{\rm unpol}(\theta,\phi)/n_{\rm unpol}}$, A_y, A_{yy}, and A_{xx} were extracted as

$$\begin{aligned} A_y(\theta) &= \frac{N'(\theta,0) - N'(\theta,\pi)}{3p_Z}, \\ A_{yy}(\theta) &= \frac{N'(\theta,0) + N'(\theta,\pi) - 2}{p_{ZZ}}, \\ A_{xx}(\theta) &= \frac{N'(\theta,-\pi/2) + N'(\theta,\pi/2) - 2}{p_{ZZ}}. \end{aligned} \tag{3}$$

This method does not require an accurate knowledge of the detector geometries and/or efficiencies of the detection system. The analyzing powers A_y, A_{yy}, and A_{xx} extracted by Eqs. (3) were averaged over three polarization modes.

In the measurement of the tensor analyzing power A_{xz}, the spin symmetry axis was rotated into the horizontal plane and inclined to $\beta = 142.2^\circ \pm 0.7^\circ$ where β is the angle between the beam direction and the spin symmetry axis by using a Wien filter system [11]. The d-p elastic scattering yields for $\phi = \pi/2$ and $-\pi/2$ (left and right) are written by using β as

$$N_{\rm pol}(\theta,\mp\pi/2) = n_{\rm pol}\,\frac{N_{\rm unpol}(\theta,\mp\pi/2)}{n_{\rm unpol}}[1 \pm \frac{1}{2}\,p_{ZZ}A_{xz}(\theta)\sin 2\beta + \frac{1}{2}\,p_{ZZ}(A_{xx}(\theta)\sin^2\beta + A_{zz}(\theta)\cos^2\beta)]\,. \tag{4}$$

A_{xz} can be extracted from these yields as

$$A_{xz}(\theta) = \frac{N'(\theta,-\pi/2) - N'(\theta,\pi/2)}{p_{ZZ}\sin 2\beta}\,, \tag{5}$$

and were averaged over three polarization modes.

The measured vector and tensor analyzing powers are plotted in Fig. 1. The error bars are statistical only. There remains a systematic error of $\pm 2\%$ from the uncertainty of the normalization of the beam polarization. A_{xz} has an additional uncertainty of $\pm 2\%$ from the uncertainty of β.

The differential cross sections were measured separately with an unpolarized deuteron beam. The diameter of the beam spot on the target was less than 2 mm. The target was a polyethylene film with a thickness of 40.5 ± 0.8 mg/cm^2. The d-p elastic scattering data were measured on the left and right sides of the beam direction by two pairs of detectors whose setup was basically the same as in the analyzing power measurement. Aluminum degraders were not used in this cross section measurement to avoid the loss of deuteron and proton flux by interactions in the degrader material. The differential cross sections are shown in Fig. 2. The statistical uncertainties, which are smaller than the size of the solid circle symbols, are within $\pm 1\%$ for all angles. Since the measured yields of left and right counters agreed within

±3%, the error arising from a geometrical misalignment of the counters, efficiencies of the data taking system, and background subtraction, is estimated to be less than ±3%. There remains a systematic error due to incomplete charge collection of the beam. It is estimated to be smaller than ±5%. The total uncertainties in the final cross section are statistical error of ±1% and a systematic error of ±6% .

It should be noted that the proton knock-out reaction from the carbon contained in the polyethylene target might influence the result of the d-p elastic scattering measurement since some of the final products of the knock-out reaction $^{12}C(d,dp)^{11}B$ are indistinguishable from those of the d-p elastic scattering. We have measured coincidence yields of deuterons and protons with a carbon target at an angle corresponding to $\theta_{c.m.} = 86.6°$ of the d-p elastic scattering. The contribution of the $^{12}C(d,dp)^{11}B$ knock-out reaction to the measured d-p elastic scattering is found to be less than 1%.

A three-body calculation with a separable expansion method [5] was performed for the d-p elastic scattering at $E_d^{lab} = 270$ MeV. The d-p scattering t-matrix is approximated by a modified d-n scattering t-matrix which is corrected for the effect of the Coulomb distortion in the manner of Ref. [12]. The d-n scattering t-matrix is obtained by solving the Faddeev equation with an NN interaction. The calculation was performed with the full two-body interactions for $j \leq 4$ involving 98 coupled channels for the scattering system. To solve the equation with a large number of coupled channels as in the present case, a separable expansion method is suitable. In the present calculation, the Argonne v_{14} potential is employed and converted to a separable series by USE. The advantage of USE is that the separable series converges quickly. By using a separable two-body t-matrix, two-dimensional integral Faddeev equations are reduced to coupled one-dimensional integral equations. The resulting one-dimensional coupled integral equations are converted to a matrix with 32-point Gaussian quadrature on a deformed contour. From the obtained matrix, a Born series is produced for the three-body on-shell scattering amplitude by using the Padé approximation which makes the Born series converge.

The results of the calculation with the NN interaction of $j \leq 3$ and those of $j \leq 4$ are

shown in Fig. 1 and 2. All components of the analyzing powers are reproduced well. Since the tensor analyzing power A_{zz}, which is known to be sensitive to the tensor part of the NN interaction at low energies, is described well, it might indicate that the tensor part of the Argonne v_{14} potential is determined adequately. Inclusion of the $j = 4$ wave slightly improves the fits of the calculated analyzing powers especially for A_{xx}. By Witala *et al.*, Faddeev calculations with $j \leq 4$ have been performed at $E_d^{lab} = 131$ MeV and 187 MeV [13]. They also reported that the inclusion of the $j = 4$ higher partial wave only slightly changes the theoretical prediction with $j \leq 3$.

In contrast, the fit to the differential cross sections is poor. The calculated cross sections are 30% smaller than the experimental values at angles around $\theta_{c.m.} = 120°$ where the cross sections have a minimum. Inclusion of the $j = 4$ partial wave does not improve the prediction obtained with $j \leq 3$. In order to see the energy dependence of this disagreement, we have performed calculations with $j \leq 3$ for deuteron incident energies of 130 MeV and 190 MeV and compared these with the existing experimental data [14,15] in Fig. 2. Note that the differential cross sections are not presented in Ref. [13]. The calculated differential cross sections are persistently smaller than the measured values. This might imply that a tuning of the Argonne v_{14} potential is needed although the analyzing powers are described well with it. Moreover, it is interesting to investigate whether the fit is improved by an explicit inclusion of the delta degrees of freedom whose effect on the three-nucleon bound state has been recently examined in Ref. [16]. Finally, it would also be interesting to study the role of relativity [17] which is one of the current issues in the study of the few nucleon systems.

In summary, differential cross sections and analyzing powers A_y, A_{yy}, A_{xx}, and A_{zz} for the d-p elastic scattering were measured at $E_d^{lab} = 270$ MeV. Three-body calculations using a separable expansion method USE were performed including the NN partial wave interactions of $j \leq 3$ and $j \leq 4$. It is found that the analyzing powers are described fairly well while the calculated differential cross sections are smaller by about 30% than the experimental values at around $\theta_{c.m.} = 120°$. A discrepancy of similar size is also found in fits to the data at lower energies, $E_d^{lab} = 130$ MeV and 190 MeV.

We would like to thank the staff of the RARF, in particular Y. Yano, for their assistance and encouragement during the experiment. We thank K. Ikegami and J. Fujita for their technical support on the RIKEN polarized ion source. We thank T. Nonaka for his help during the cross section measurement. One of the authors, N. S., acknowledges valuable discussions with A. Itabashi, M. B. Greenfield, and S. Oryu. Data analysis was performed with the VAX6610 computer system of RIKEN. Theoretical calculations were performed with the work station IBM7006-41T of Hosei University. This work is supported in part by JSPS Fellowships for Japanese Junior Scientists and also supported financially in part by the Grant-in-Aid for Scientific Research No. 04402004 of Ministry of Education, Science and Culture of Japan.

REFERENCES

[1] W. Glöckle *et al.*, AIP Conference Proceedings **334**(1994) p.45.

[2] K. Dow *et al.*, Phys. Rev. Lett. **61**(1988)1706.

[3] S. Ishikawa *et al.*, Phys. Lett. **B339**(1994)293.

[4] R. B. Wiringa, R. A. Smith, and T. A. Ainsworth, Phys. Rev. **C29**(1984)1207.

[5] Y. Koike *et al.*, AIP Conference Proceedings **334**(1994) p.836.

[6] Y. Koike, W. C. Parke, L. C. Maximon and D. R. Lehman, in preparation.

[7] N. Sakamoto *et al.*, RIKEN Accel. Prog. Rep. **26**(1992)138.

[8] H. Okamura *et al.*, AIP Conference Proceedings **293**(1993) p.84.

[9] Proc. of the third Int. Conf. on polarization phenomena in nuclear reactions, eds. H. H. Varschall and W. Haeberli (Univ. Winsconsin Press, Madison 1971).

[10] G. G. Ohlsen, Rep. Prog. Phys. **35**(1972)717; G. G. Ohlsen and P. W. Keaton, Jr., Nucl. Instr. and Meth. **109**(1973)41.

[11] H. Okamura *et al.*, contribution to SPIN'94 at Bloomington, 1994. to be published in AIP Conference Proceedings.

[12] W. Grübler, Nucl. Phys. **A353**(1981)31c.

[13] H. Witala *et al.*, Few Body Systems **15**(1993)67.

[14] H. Shimizu *et al.*, Nucl. Phys. **A382**(1982)242.

[15] O. Chamberlain and M. O. Stern, Phys. Rev. **94**(1954)666.

[16] CH. Hajduk and P. U. Sauer, Nucl. Phys. **A322**(1979)329; A. Stadler and P. U. Sauer, Phys. Rev. **C46**(1992)64; A. Picklesimer, R. A. Rice, and R. Brandenburg, Few Body Systems **19**(1995)47.

[17] J. A. Tjon, AIP Conference Proceedings **334**(1994) p.177.

FIGURES

FIG. 1. The vector and tensor analyzing powers for the d-p elastic scattering at $E_d^{\text{lab}} = 270$ MeV. The error bars are statistical ones only. Dashed and solid curves are the results of Faddeev calculations with the Argonne v_{14} N-N interaction for $j \leq 3$ and $j \leq 4$, respectively.

FIG. 2. The differential cross sections for the d-p elastic scattering at $E_d^{\text{lab}} = 130$ MeV [14], 190 MeV [15], and 270 MeV (present data). The systematic errors are not shown in the figure. Solid and dashed curves are the same as in Fig. 1.

N. Sakamoto
Physics Letters B

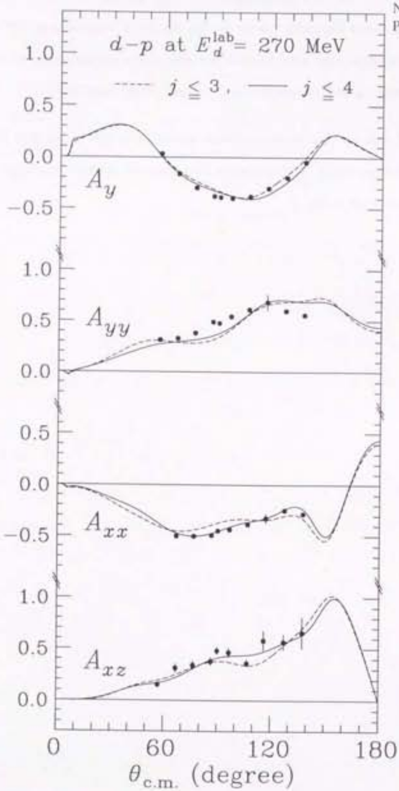

Fig. 1

N. Sakamoto
Physics Letters B

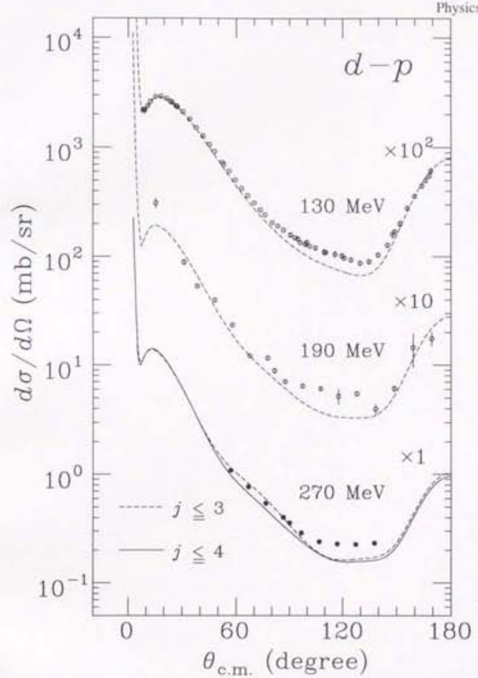

Fig. 2